

Empirical evaluation of normalizing flows in Markov Chain Monte Carlo

David Nabergoj

*University of Ljubljana
Faculty of Computer and Information Science
Večna pot 113, 1000 Ljubljana, Slovenia*

DAVID.NABERGOJ@FRI.UNI-LJ.SI

Erik Štrumbelj

*University of Ljubljana
Faculty of Computer and Information Science
Večna pot 113, 1000 Ljubljana, Slovenia*

ERIK.S@FRI.UNI-LJ.SI

Abstract

Recent advances in MCMC use normalizing flows to precondition target distributions and enable jumps to distant regions. However, there is currently no systematic comparison of different normalizing flow architectures for MCMC. As such, many works choose simple flow architectures that are readily available and do not consider other models. Guidelines for choosing an appropriate architecture would reduce analysis time for practitioners and motivate researchers to take the recommended models as foundations to be improved. We provide the first such guideline by extensively evaluating many normalizing flow architectures on various flow-based MCMC methods and target distributions. When the target density gradient is available, we show that flow-based MCMC outperforms classic MCMC for suitable NF architecture choices with minor hyperparameter tuning. When the gradient is unavailable, flow-based MCMC wins with off-the-shelf architectures. We find contractive residual flows to be the best general-purpose models with relatively low sensitivity to hyperparameter choice. We also provide various insights into normalizing flow behavior within MCMC when varying their hyperparameters, properties of target distributions, and the overall computational budget.

Keywords: normalizing flow, Markov Chain Monte Carlo, comparison, sampling, simulation study

1 Introduction

In recent years, many works have used normalizing flows (NF) within Markov Chain Monte Carlo (MCMC) to accelerate distribution sampling in lattice field theory (Del Debbio et al., 2021; Matthews et al., 2022; Abbott et al., 2023), molecular dynamics (Wu et al., 2020; Arbel et al., 2021; Matthews et al., 2022), gravitational wave analyses (Karamanis et al., 2022; Williams et al., 2021), general Bayesian model posteriors (Hoffman et al., 2019; Grunmitt et al., 2022, 2024), and other fields. NF-based MCMC (NFMC) approaches typically either transform a geometrically complex target distribution into a simple one that is more amenable to MCMC sampling (Hoffman et al., 2019) or replace some MCMC steps with independent sampling from an NF, which facilitates transitions to distant parts of the sampling space (Samsonov et al., 2024). These enhancements allowed researchers to obtain satisfactory analysis results compared to classic MCMC. Still, many papers use specific

combinations of MCMC samplers and NF architectures for their target distribution. A recent paper discusses some practical differences between NFMC samplers (Grenieux et al., 2023). In Section 2, we list several NFMC works and highlight key observations regarding NF properties within NFMC. Many of these propose NFMC and NF combinations for their specific problem but do not thoroughly evaluate existing methods or compare them to other NFMC and MCMC methods. The lack of systematic evaluation and comparison hinders the adoption of NFMC for sampling and leaves some key questions unanswered:

1. When does NFMC accelerate sampling over MCMC?
2. When NFMC is the better choice, which combination of sampler and NF architecture is best?

The first question is crucial to understanding when to invest time in configuring the more complex NFMC samplers. The second question deals with choosing a suitable initial sampler-NF combination and saving time otherwise spent trying different, possibly unsuitable methods. Answering these questions would substantially speed up research and analysis workflows that rely on NFMC while introducing the field to a broader audience that does not necessarily have the expertise required to select appropriate sampler-NF combinations. Since NFs are largely black box models based on deep neural networks, a suitable way to answer these questions is empirically.

We answer the first question by evaluating different NF architectures and NFMC samplers on various target distributions and then comparing results to MCMC. We answer the second question by narrowing our analysis to contexts where NFMC is superior to MCMC and then performing a detailed comparison of NFs within NFMC. We state which NFMC-NF combination is the best choice in general and for families of similar distributions, as well as what NF properties are correlated with good sampling performance.

We investigate architectures in the family of autoregressive, residual, and continuous NFs, including popular models like Real NVP (Dinh et al., 2017), MAF (Papamakarios et al., 2017) and IAF (Kingma et al., 2016), neural spline flows (Durkan et al., 2019, NSF), invertible ResNets (Behrmann et al., 2019, i-ResNet), continuous NFs (Grathwohl et al., 2018; Salman et al., 2018), and others. We first consider Metropolis-Hastings (MH) and Hamiltonian Monte Carlo (HMC) as classic MCMC baselines when the target log density gradients are unavailable and available, respectively. We then augment each in two separate ways: by preconditioning the target according to NeuTra MCMC (Hoffman et al., 2019) and by replacing some MCMC steps with independent NF jumps according to Local-Global MCMC (Samsonov et al., 2024), which we term *Jump MCMC*, abbreviating the MH version as Jump MH and HMC version as Jump HMC. As a special case of Jump MH, we consider the independent Metropolis-Hastings sampler (Samsonov et al., 2024; Brofos et al., 2022, IMH), which proposes the new state at each step as a sample from an NF. We compare NFMC and NF methods on a custom benchmark consisting of four target distribution families: synthetic Gaussians, synthetic unimodal non-Gaussians, synthetic multimodal targets, and real-world distributions consisting of commonly analyzed Bayesian model posteriors. In Section 3, we describe in detail all considered NF architectures, samplers, target distributions, and our comparison methodology.

2 Related work

The most relevant work is by Grenioux et al. (2023), who analyze NeuTra MCMC, Jump MCMC, and NF-based importance sampling. They conclude that NeuTra MCMC is generally superior to Jump MCMC but does not mix between target modes. They also state that NFMC performance drops with increasing target dimensionality, with Jump MCMC being the most affected by this. However, they draw their conclusions based on only one or two synthetic targets per experiment and only four autoregressive NF architectures, which limits generalization. We build on their work by increasing the number of NF architectures with representatives from different NF families, as well as the suite of both synthetic and real-world target distributions.

A recent analysis finds that IMH outperforms the Metropolis-adjusted Langevin algorithm (MALA) on a 50D Gaussian process, a 2D multimodal target, and a multimodal lattice field theory target (Brofos et al., 2022). Other works also find that IMH improves upon MCMC in field theory analyses (Albergo et al., 2019; Del Debbio et al., 2021), with Abbott et al. (2023) noting that scaling and scalability are affected by the choice of sampler hyperparameters, NF architecture, and NF hyperparameters. However, numerical experiments in these works mainly consider field theory examples and use at most a few NF architectures. Furthermore, they focus on multimodal distributions, whereas IMH could also be applied to other targets. Hoffman et al. (2019) state that sampling quality in NeuTra MCMC depends on the NF fit and that poor fits could lead to slow mixing in the tails, but only consider the IAF architecture without investigating sensitivity to hyperparameters or other architectures. Samsonov et al. (2024) show that interleaving MALA with Real NVP jumps explores a 50D multimodal target and a 128D latent space of a generative adversarial network target better than either sampler alone. Their approach outperforms the no-U-turn sampler (Hoffman and Gelman, 2011, NUTS) on the funnel and Rosenbrock distributions in low-to-moderate dimensions but performs worse in high dimensions.

There are a number of findings for NF-based particle transport methods. Karamanis et al. (2022) state that their method is useful for computationally expensive targets, targets with highly correlated dimensions, and multimodal targets. However, they only consider the MAF architecture in their experiments. Grumitt et al. (2022) also apply their method to computationally expensive targets and find that small learning rates increase NF robustness for targets with complicated geometries. Grumitt et al. (2024) suggest using NF architectures with good inductive biases for common target geometries, e.g., in hierarchical Bayesian models, but do not state specific architectures or empirically explore this idea. Wu et al. (2020) find NSF to be comparable or more expressive than the commonly used Real NVP for particle transport, which suggests that NFMC methods would benefit from more careful architecture choices. They also find that their NFMC method improves upon MCMC for the double well and alanine dipeptide multimodal test cases. Arbel et al. (2021) and Matthews et al. (2022) build on this work, but both only consider the Real NVP architecture.

In summary, the field lacks clarity with respect to choosing an appropriate NF architecture and lacks an answer as to when NFMC is even a suitable alternative to MCMC. Rough guidelines exist for the latter (low-to-moderate dimensional, multimodal, non-Gaussian, or

computationally expensive targets), but they are not verified with a thorough empirical evaluation across many targets and NF architectures.

3 Methods

In this section, we list the analyzed MCMC methods and NF architectures. We also describe the target distributions in the benchmark and our comparison methodology.

3.1 Samplers

We first aim to show that adding NFs to MCMC can improve its performance through independent jumps or preconditioning. To eliminate some sources of variance within our experiments, we first limit ourselves to MCMC samplers with established and stable kernel tuning procedures. We focus on NeuTra MCMC and Jump MCMC as they are direct extensions of MCMC without additional sampler components. They let us assess the preconditioning and jump performance of NFs in a controlled manner. Methods like NUTS are very successful in practice. However, NUTS presently has no NeuTra MCMC or Jump MCMC extensions and theoretically developing these is beyond the scope of our paper. Furthermore, it has already been compared to NFMC in previous works (Samsonov et al., 2024; Grumitt et al., 2022). Due to the large number of both NF architectures and target distributions in the benchmark, evaluating many MCMC samplers would also lead to an even greater combinatorial explosion in the number of experiments.

We thus limit ourselves to MH as the gradient-free MCMC representative and HMC as the gradient-based one. Besides being used in various practical analyses, their NeuTra MCMC and Jump MCMC extensions have also been theoretically analyzed (Brofos et al., 2022; Samsonov et al., 2024; Hoffman et al., 2019), which facilitates the understanding and discussion of experiments in our work. Our results thus enrich the past assessments of these methods with a broader range of NF architectures. We also provide many new empirical results for Jump MH and NeuTra MH, which are not commonly used but fit exactly into the frameworks defined by Samsonov et al. (2024) and Hoffman et al. (2019). Our results may encourage their use in practical gradient-free analyses.

All samplers we investigate are Metropolis methods. Such methods start with an initial state for each chain, then iteratively propose new states and apply the Metropolis accept/reject rule to generate samples and compute distribution moments. In the rest of this section, we list the investigated NF-based samplers for preconditioning and global exploration, as well as MH and HMC samplers that underlie these NFMC methods. We further describe the investigated samplers in Appendix C.

3.1.1 NEUTRA PRECONDITIONING

For preconditioning, we consider the NeuTra method (Hoffman et al., 2019). Instead of sampling from the target density p , NeuTra MCMC adjusts p with a bijection f and samples from the adjusted density. After MCMC, we transform the sampled points with f^{-1} , yielding the samples from the target density. The adjusted log density is defined as:

$$\log \tilde{p}(x) = \log p(f(x)) + \log \left| \det \left(\frac{\partial f(x)}{\partial x} \right) \right|. \quad (1)$$

The bijection f is associated with an NF, which is fit to $\log p$ with stochastic variational inference (SVI; see Rezende and Mohamed, 2015, for application with NFs). After SVI, the NF remains fixed and we proceed with sampling from the adjusted density. Given a fixed computational budget, the challenge is training NFs well enough to outperform MCMC despite being unable to adjust f during sampling.

3.1.2 LOCAL MCMC AND GLOBAL NF PROPOSALS

Another approach to using NFs within MCMC is replacing some MCMC proposals with independent sampling from an NF (Samsonov et al., 2024). We term this Jump MCMC as independent sampling with a global NF proposal amounts to *jumping* to different parts of space to continue MCMC exploration. The most straightforward approach is to replace the MCMC proposal with an independent sample from an NF q every K -th iteration. Assume the chain is at iteration t , divisible by K . The proposal and log acceptance probability are:

$$x'_{t+1} \sim q(x_t), \tag{2}$$

$$\log \alpha_t = \log p(x'_{t+1}) - \log p(x_t) + \log q(x_t) - \log q(x'_{t+1}). \tag{3}$$

When $K = 1$, we use an independent NF proposal at every iteration, which corresponds to the IMH sampler. Whereas Jump MCMC combines global NF samples with local MCMC exploration, IMH uses solely NF-based jumps. This can be beneficial if the NF approximates the target density well and the local MCMC fails to explore the space adequately. An example where IMH is the better choice is finding mode weights of a multimodal distribution with strongly separated peaks. Since our primary interest is finding how many particles fall into a particular mode, we do not care how well the modes are explored, so standard MCMC steps do not benefit us. The challenge is again to find an NF that approximates the target density well enough to jump between regions of space more quickly than MCMC trajectories.

When investigating NFs in these aspects, we consider two scenarios that govern which underlying MCMC samplers are sensible choices. First, we consider the case where the target log density gradient is unavailable. Such cases are found in, e.g., cosmology (Karamanis et al., 2022) or simulations of physical systems (Grumitt et al., 2024), as many existing codes for dynamical system simulations are not differentiable despite recent efforts to change this (Schoenholz and Cubuk, 2021). Second, we consider cases where the target log density has an available gradient. This covers many different Bayesian model posteriors (Agrawal and Domke, 2024; Hoffman et al., 2019) and recent work in lattice field theory (Albergo et al., 2019).

3.1.3 OTHER NFMC SAMPLERS

We acknowledge NFMC samplers such as Deterministic Langevin Monte Carlo (Grumitt et al., 2022, DLMC), Transport elliptical slice sampling (Cabezas and Nemeth, 2023, TESS), and Nested sampling (Williams et al., 2021, NS), however we choose to exclude them from our experiments. We justify this as follows:

- MH and HMC are already suitable for a fair comparison of NF architectures and have a simpler, extensively tested kernel-tuning procedure that is less prone to errors.

- Comparing MH/HMC performance to their NFMC analogs lets us determine when NFMC is better than MCMC while observing changes after adding preconditioning and NF jumps without otherwise affecting underlying MCMC dynamics. However, no such analog exists for DLMC. DLMC also mixes jump proposals with preconditioning, hindering our investigation of which approach is more efficient.
- We omit NS as it relies on an extensive sampling pipeline that requires additional hyperparameter considerations.
- We omit TESS as a gradient-free representative, as the underlying dynamics of elliptical slice sampling are more complex and more challenging to analyze than simple MH dynamics.

We also acknowledge NFMC methods with roots in sequential Monte Carlo (Karamanis et al., 2022; Wu et al., 2020; Arbel et al., 2021; Matthews et al., 2022) and importance sampling (Midgley et al., 2023). However, the former methods rely on a more extensive set of hyperparameters (including careful target-dependent temperature scheduling), while the latter is not technically an MCMC method.

3.2 Normalizing flow architectures

An NF is a distribution defined as a transformation of a simple distribution p_Z into a complex distribution p_X with a bijection f . Sampling from an NF is equivalent to sampling $z \sim p_Z$ and transforming the sample with $x = f^{-1}(z)$, while $\log p_X$ is computed as:

$$\log p_X(x) = \log p_Z(f(x)) + \log \left| \det \left(\frac{\partial f(x)}{\partial x} \right) \right|. \quad (4)$$

This expression is similar to Equation 1, which maps the target distribution to a transformed target via a bijection f . The bijection is most commonly parameterized by deep neural networks. The difference is in our base distribution and intended use: Equation 1 transforms the target log density into a density that is easier to sample. Equation 4 transforms a simple distribution into a complex one that acts as a global proposal distribution or whose bijection f preconditions a target density. Papamakarios et al. (2021) reviewed a large number of NF architectures, all defined using Equation 4, and identified three main NF families with different approaches to constructing f . We describe these families in the following subsections and list the architectures we investigate.

3.2.1 AUTOREGRESSIVE NFs

The first family consists of autoregressive architectures, where f is a composition of invertible deep bijections f_i and the Jacobian of f is triangular. The functions f_i are typically either coupling bijections or masked autoregressive (MA) bijections.

Coupling bijections receive an input x and partition it into disjoint inputs (x_A, x_B) . The output $f_i(x) = y$ is partitioned into (y_A, y_B) on the same dimensions. Part B stays constant ($y_B = x_B$) while y_A is computed as $y_A = \tau(x_A; \phi(x_B))$, where τ is a *transformer* – a bijection, parameterized with $\phi(x_B)$. The function ϕ is a *conditioner*, which takes one of the vectors as input and predicts the parameters for τ . Coupling bijections are autoregressive as each dimension of y is a function of the corresponding preceding dimensions in x . y_A trivially stays constant, while y_B is transformed using the preceding x_A . For the same

reason, their Jacobian is also triangular and its determinant can be computed efficiently. The function ϕ need not be bijective, so we make it a deep neural network, which makes f_i expressive. The composition f thus accurately models complex distributions provided ϕ is sufficiently complex and the number of bijections f_i is sufficiently large (Draxler et al., 2024; Lee et al., 2021). We compose coupling bijections with permutations (also bijections) to avoid repeatedly using the same dimensions in parts A and B. This also means the dimension order can be arbitrary when analyzing the Jacobian.

MA bijections explicitly compute each output dimension as a function of *all* preceding input dimensions. This also holds for inverse autoregressive (IA) bijections, which are the inverses of MA bijections. This is in contrast to coupling bijections, which retain the autoregressive property by partitioning the input and thus cleverly ignoring specific dimensions. MA bijections achieve this with a Masked Autoencoder for Distribution Estimation (Germain et al., 2015, MADE) as the conditioner. MADE maps a d -dimensional input to a d -dimensional output with an autoencoder whose weights are masked to retain the autoregressive property between layers and thus in the entire neural network. All coupling bijection transformers are compatible with MA bijection transformers and vice-versa. The drawback of MA bijections is that their inverse pass requires $\mathcal{O}(d)$ operations. This results in poor scaling with data dimensionality when we need to perform both the forward and inverse passes.

Each coupling and MA bijection consists of a transformer and a conditioner. For thoroughness, we investigate all combinations of the following:

- For transformers, we consider shift (Dinh et al., 2015, used in NICE), affine map (Dinh et al., 2017, used in Real NVP), linear rational spline (Dolatabadi et al., 2020, LRS), rational quadratic spline (Durkan et al., 2019, RQS), and invertible neural networks (Huang et al., 2018, used in NAF): NN_{deep} , NN_{dense} , and NN_{both} , corresponding to neural networks that are (1) deep and thin, (2) shallow and dense, and (3) deep and dense.
- For conditioners, we use (1) a coupling conditioner that splits an input tensor in half according to its first dimension and uses a feed-forward neural network to predict transformer parameters and (2) a MADE conditioner.

We denote all coupling architectures with the “C-” prefix and all IA architectures with the “IA-” prefix. We investigate IA architectures instead of MA architectures as the former have efficient inverses, which is necessary for NeuTra MCMC. We do not investigate MA architectures, as they have efficient forward but inefficient inverse passes. This property is not useful for any investigated NFMC sampler. We provide further details on conditioner and transformer hyperparameters in Appendix B.4.

3.2.2 RESIDUAL NFS

Residual bijections map an input according to $f_i(x) = x + g_i(x)$, where g outputs a residual value. The transformation in residual NFs is a composition of such bijections. A sufficiently long composition ensures that x can gradually be transformed into a desired data point using small residual values. We place the investigated residual NFs into one of two categories: architectures based on the matrix determinant lemma and contractive residual architectures that incrementally transform data with contractive maps.

For residual architectures based on the matrix determinant lemma, the determinant of f_i can be efficiently computed via the following equation:

$$\det \left(\frac{\partial f_i(x)}{\partial f} \right) = \det \left(I + W^\top A^{-1}V \right) \det A = \det \left(A + VW^\top \right).$$

We investigate three architectures following this lemma: planar flows (Rezende and Mohamed, 2015), Sylvester flows (Berg et al., 2018), and radial flows (Tabak and Turner, 2013; Rezende and Mohamed, 2015), with the following functions and determinants in each layer:

$$\begin{aligned} g_p(x) &= v\sigma(w^\top x + b), & \det \left(\frac{\partial f_p(x)}{\partial x} \right) &= I + s(x)vw^\top; \\ g_s(x) &= V\sigma(W^\top x + b), & \det \left(\frac{\partial f_s(x)}{\partial x} \right) &= I + S(x)VW^\top; \\ g_r(x) &= \frac{\beta(x - x_0)}{\alpha + r(x)}, & \det \left(\frac{\partial f_r(x)}{\partial x} \right) &= I + \frac{\beta}{\alpha + r(x)} \left(I - \frac{(x - x_0)(x - x_0)^\top}{r(x)(\alpha + r(x))} \right). \end{aligned}$$

The subscripts p, s, r correspond to planar, Sylvester, and radial flows. We define $r(x) = \|x - x_0\|_2$, $s(x) = \sigma'(w^\top x + b)$, $S(x) = \sigma'(W^\top x + b)$, where σ is the sigmoid function.

Contractive residual architectures are also compositions of residual bijections. They use contractive maps as the functions g_i . A map is contractive with respect to a distance function δ if there exists a constant $L < 1$ such that $\delta(f_i(x), f_i(y)) \leq L\delta(x, y)$ for any $x, y \in \mathbb{R}^d$. By the Banach fixed point theorem (Behrmann et al., 2019), any contractive map has one fixed point $x_* = f_i(x_*)$, which we obtain by starting with an arbitrary x_1 and repeatedly applying $x_{k+1} = f_i(x_k)$. This lets us compute the inverse of f_i as well. The update $x_{k+1} = x' - g_i(x_k)$ is guaranteed to converge to $x_* = f_i^{-1}(x')$ for any starting point x_1 . We can compute an unbiased estimate of the log determinant with the Hutchinson trace estimator (Hutchinson, 1989) within a power series (Behrmann et al., 2019):

$$\log \left| \det \left(\frac{\partial f_i(z)}{\partial z} \right) \right| = \sum_{i=1}^{\infty} \frac{(-1)^{k+1}}{k} \text{Tr} \left(\frac{\partial g_i(z)}{\partial z} \right) \approx \sum_{j=1}^n \frac{(-1)^{k+1}}{k} w_j^\top \frac{\partial g_i(z)}{\partial z} w_j,$$

where $w_j \sim \mathcal{N}(0, I)$. We alternatively compute the series with the Russian roulette estimator (Chen et al., 2019):

$$\sum_{i=1}^{\infty} \frac{(-1)^{k+1}}{k} \text{Tr} \left(\frac{\partial g_i(z)}{\partial z} \right) \approx \mathbb{E}_{n,w} \left[\sum_{k=1}^n \frac{(-1)^{k+1}}{k} w_j^\top \left(\frac{\partial g_i(z)}{\partial z} \right)^k w_j / P(N \geq k) \right].$$

We investigate the difference between the two by evaluating both i-ResNet that uses the power series estimator and the residual flow (Chen et al., 2019, ResFlow) that uses the Roulette estimator. Both construct g_i as neural networks with spectral regularization to ensure $L < 1$, which makes the maps contractive. We provide neural network parameterization details in Appendix B.4.

3.2.3 CONTINUOUS NFs

Lastly, we consider continuous NF architectures. Unlike autoregressive and residual architectures, which are compositions of a finite number of layers, continuous NFs transform

points between latent and target spaces by simulating an ordinary differential equation (ODE). This continuously maps a latent point $z = z_0 \sim p_Z$ from time t_0 to a target data point $x = z_1 = f^{-1}(z_0)$ at time t_1 . We compute the target point and log determinant as:

$$z_1 = z_0 + \int_{t_0}^{t_1} g_\phi(t, z_t), \log \left| \det \left(\frac{\partial f^{-1}(z_0)}{\partial z_0} \right) \right| = - \int_{t_0}^{t_1} \text{Tr} \left(\frac{\partial g_\phi(t, z_t)}{\partial z_t} \right), \quad (5)$$

where the neural network $g_\phi : \mathbb{R} \rightarrow \mathbb{R}$ determines the ODE: $g_\phi(t, z_t) = \frac{\partial z_t}{\partial t}$. To compute the latent point, we subtract the integral in Equation 5 (left) from both sides. Similarly, we omit the minus sign in Equation 5 (right) to obtain the log determinant of $f(z_1)$ with respect to z_1 . We compute the integrals using numerical solvers. The integrals for point and log determinant computation can be computed jointly by combining the two ODEs in \mathbb{R}^d into a single one in \mathbb{R}^{2d} .

We investigate three kinds of continuous NFs with different ways of solving the integral in Equation 5 and different specifications of neural networks g_ϕ :

- CNF_{Euler}, which approximates the integral with the Euler-Maruyama solver in 150 steps (Salman et al., 2018) and parameterizes g_ϕ as a time-independent feed-forward network.
- CNF_{RK}, which approximates the integral with the adaptive Runge-Kutta 4(5) solver (Grathwohl et al., 2018; Finlay et al., 2020) and parameterizes g_ϕ with a time-dependent neural network.
- CNF_{RK(R)}, which is the same as CNF_{RK}, but regularizes g_ϕ by the squared norm of the Jacobian of its transformation (Grathwohl et al., 2018).

All three methods use the Hutchinson trace estimator to compute an unbiased estimate of the trace and avoid costly deterministic computations:

$$\text{Tr} \left(\frac{\partial f(x)}{\partial x} \right) \approx \frac{1}{n} \sum_{i=1}^n w_i^\top \text{Tr} \left(\frac{\partial f(x)}{\partial x} \right) w_i, w_i \sim \mathcal{N}(0, I),$$

where the sum is computed efficiently using Jacobian-vector products. CNF_{Euler} solves the ODE in a finite number of steps with the Euler-Maruyama method, which can create significant errors compared to more advanced ODE solvers but is very fast to evaluate. Conversely, the adaptive Runge-Kutta 4(5) solver provides more accurate log density estimates and precise samples but can be expensive to evaluate. We provide neural network parameterization details in Appendix B.4.

3.3 Benchmark target distributions

We consider synthetic and real-world target distributions in our benchmark, which we describe in the following sections. Our benchmark includes various commonly analyzed targets and partly overlaps with the recently described NF benchmark for SVI (Agrawal and Domke, 2024).

3.3.1 SYNTHETIC TARGETS

Synthetic targets let us evaluate NFs in scenarios that mimic regions of real-world distributions.

If our target distribution is approximately Gaussian, it is beneficial to focus on NFMC and NF methods with good performance on actual synthetic Gaussians. We include four such 100D distributions in our benchmark: standard Gaussian, diagonal Gaussian, full-rank Gaussian, and ill-conditioned full-rank Gaussian. The mean of all targets is zero in each dimension. Eigenvalues for diagonal and full-rank Gaussians are linearly spaced between 1 and 10. Reciprocals of eigenvalues for the ill-conditioned full-rank Gaussian are sampled from $\text{Gamma}(0.5, 1)$, making the condition number of the covariance matrix high and causing sampling from this target to be difficult. We provide details on full-rank Gaussians in Appendix D.1.

Hierarchical Bayesian models are common ways of modeling real-world phenomena and often use priors with spatially varying curvature (Grumitt et al., 2022, 2024). Sampling from such priors is complex, which leads to long MCMC runs when we have few data points for the likelihood. We include the 100D funnel and 100D Rosenbrock distributions in our benchmark to facilitate choosing sampling methods in this scenario. The funnel distribution and the unnormalized Rosenbrock log density are respectively defined as:

$$x_1 \sim \mathcal{N}(0, 3); x_i | x_1 \sim N(0, \exp(x_1/2))$$

$$\log \tilde{p}(x) = - \sum_{d=1}^{D/2} s(x_{2d-1}^2 - x_{2d})^2 + (x_{2d-1} - 1)^2,$$

where D is even and $s > 0$ is a fixed scale parameter.

Many NFMC and NF methods were proposed to sample from multimodal distributions. To evaluate NFMC methods and NFs in such cases, we include the following targets in our benchmark:

- 100D Gaussian mixture with three components, equal weights.
- 100D Gaussian mixture with 20 components, random weights.
- 10D double well distribution with 2^{10} modes.
- 100D double well distribution with 2^{100} modes.

The unnormalized double well density is defined as $\log \tilde{p}(x) = - \sum_{d=1}^D (x^2 - 4)^2$. We provide details on target definitions in Appendix D.3. We view these distributions as increasingly complex due to their growing number of components and modes. A successful sampling method will retain good performance regardless of the number of modes.

3.3.2 REAL-WORLD BAYESIAN MODEL POSTERiors

We include diverse Bayesian model posterior distributions that describe real-world phenomena. These are also commonly used for MCMC benchmarking (Magnusson et al., 2024):

- 10D Eight schools target, which models the effectiveness of coaching programs for standardized college admission tests based on scores from eight schools.
- 25D German credit and 51D sparse German credit targets, which model credit risk.
- Two 89D targets and one 175D target, which model the concentration of radon in Minnesotan households.
- 501D synthetic item response theory target, which models the process of students answering questions.
- 3003D stochastic volatility target, which models evaluation of derivative securities, such as options.

We provide precise distribution definitions in Appendix D.4.

3.4 Evaluation methodology

We compare samplers and NFs in estimating the second moment of the target with a given computational budget. We use the squared bias of the second moment as the comparison metric, shortened as b^2 . Using b^2 relates our experiments to other works in NFMC, as it is a commonly used metric in the field (see e.g., Hoffman et al., 2019; Grumitt et al., 2022).

When comparing methods across different targets, b^2 cannot be naively compared due to different true second moments. We thus opt for a rank standardization approach (Urbano et al., 2019). We rank different methods from minimum to maximum b^2 on each target. We compute standardized ranks (SR) on each target, then observe a method’s empirical average rank \bar{r} and standard error of the mean $\hat{\sigma}$ as an uncertainty estimate. This ensures that all methods are comparable across all targets. We choose not to transform SR to the $[0, 1]$ interval as in (Urbano et al., 2019) because it would result in skewed uncertainties that are difficult to interpret. We provide a detailed definition of SR in Appendix E.

Each NFMC experiment consists of a target distribution, NFMC sampler, NF architecture, and the corresponding set of NF hyperparameters. When comparing NFs, we consider two main cases when analyzing each experiment:

- We observe b^2 when using the default NF hyperparameter set for the used architecture.
- We observe b^2 when using the NF hyperparameter set that yields the smallest b^2 among all hyperparameter sets on that experiment.

We choose the default hyperparameters as follows: we run all experiments with six different hyperparameter sets. We then count the number of times each hyperparameter set attains the smallest b^2 across all experiments. The set with the highest count is marked as the default. By analyzing the results of experiments with default hyperparameters, we obtain estimates of how architectures will behave in new experiments without any hyperparameter tuning. By analyzing results that pertain to the smallest b^2 , we obtain best-case performance estimates for different architectures.

4 Results

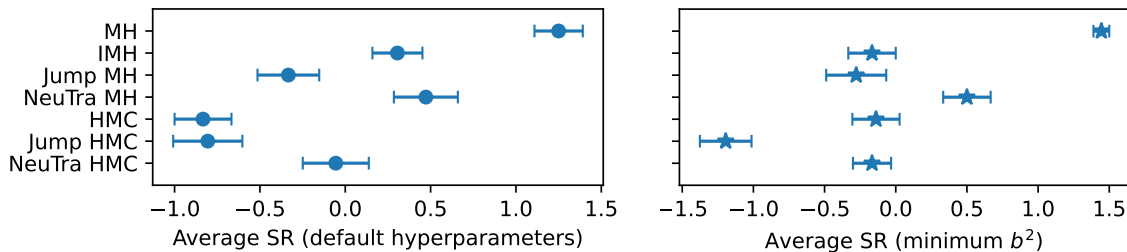
In this section, we show our main sampler and NF comparison results. For every experiment, we warm up the sampler for 3 hours and sample for 8 hours to ensure each NF has enough time and data to attain a good fit. In Appendix A, we provide additional results regarding NF operation speed and differences between autoregressive NF components, as well as experiments with short NFMC runs. We provide all experiment configuration details in Appendix B.1.

4.1 MCMC vs NFMC

We show that NFMC can outperform MCMC despite using NF models with many trainable parameters. We provide a short summary of our findings at the end of this section.

4.1.1 SAMPLER COMPARISON ACROSS ALL TARGETS AND NFS

In Figure 1a, we compare MCMC with NFMC in terms of SR based on experiments with default NF hyperparameters.



(a) $\bar{r} \pm \hat{\sigma}$ across all targets and NFs for each sampler, using b^2 limited to experiments with default NF hyperparameters.

(b) $\bar{r} \pm \hat{\sigma}$ across all targets and NFs for each sampler, values estimated with minimum b^2 across all NF hyperparameter sets.

In the gradient-based setting, the differences between HMC and Jump HMC are negligible. In the worst case, most jumps are either rejected, or states visited in this way do not contribute to moment estimates any more than HMC dynamics. NeuTra HMC performs more poorly than HMC and Jump HMC, suggesting that HMC exploration is generally hindered by NF preconditioning when NF hyperparameters are not tuned.

In the gradient-free setting, IMH, Jump MH, and NeuTra MH all outrank MH. This suggests that preconditioning and jumps both improve MH dynamics. Finding a balance between jumps and MH transitions is preferable to independent jumps or standard MH, as indicated by Jump MH outperforming both IMH and MH. Both Jump HMC and Jump MH outrank their NeuTra counterparts, with Jump MH also being better than NeuTra HMC. Independent NF jumps enable better exploration than NF-based preconditioning.

In Figure 1b, we compare samplers by their best attainable sampling performance. Jump HMC outranks all other samplers. Each jump-based sampler again outranks its MCMC and NeuTra MCMC counterparts, which agrees with our previous findings that jumps are preferable to preconditioning. Even with a suitable NF architecture and hyperparameters, NeuTra HMC only matches the performance of HMC and does not improve on it. Despite being gradient-free samplers, IMH and Jump MH also potentially outrank or at least match HMC, which further demonstrates the benefits of independent jumps.

4.1.2 BEST-CASE ANALYSIS FOR SPECIFIC TARGET FAMILIES

We compare samplers when applied to different families of target distributions in Table 1.

Jump HMC ranks best on each family and is tied with Jump MH on non-Gaussian unimodal targets. In gradient-free sampling, Jump MH performs best on synthetic targets, while IMH is better on real-world targets. Hoffman et al. (2019) show that NeuTra HMC explores geometrically complex targets more efficiently than HMC. However, we find their ranks to be the same on non-Gaussian targets. Due to the high uncertainty in HMC, it is plausible that some NFs allow NeuTra HMC to rank better, though this is not the case in general. Moreover, NeuTra HMC is actually worse for Gaussian targets and does not improve results in general (see Figures 1a and 1b).

Sampler	Gaussian	Non-Gaussian	Multimodal	Real-world	All
MH	1.5	1.5	1.5	1.38 ± 0.12	1.44 ± 0.06
IMH	0.38 ± 0.47	0.00 ± 0.50	0.25 ± 0.25	-0.69 ± 0.09	-0.17 ± 0.17
Jump MH	-0.50 ± 0.29	-1.25 ± 0.25	-0.75 ± 0.32	0.31 ± 0.31	-0.28 ± 0.21
NeuTra MH	0.75 ± 0.14	1.0	0.50 ± 0.50	0.25 ± 0.27	0.50 ± 0.17
HMC	-0.62 ± 0.12	0.00 ± 0.50	-0.12 ± 0.43	0.06 ± 0.27	-0.14 ± 0.17
Jump HMC	-1.5	-1.25 ± 0.25	-1.38 ± 0.12	-0.94 ± 0.39	-1.19 ± 0.18
NeuTra HMC	0.00 ± 0.20	0.0	0.00 ± 0.20	-0.38 ± 0.26	-0.17 ± 0.13

Table 1: $\bar{r} \pm \hat{\sigma}$ for all samplers and target families. Samplers with the best \bar{r} are shown in bold for each target family. We estimate $\bar{r} \pm \hat{\sigma}$ with the minimum b^2 across all NFs for each target within a family. Entries without $\hat{\sigma}$ always attain the same \bar{r} . Ranks are computed separately for each target family.

4.1.3 SHORT SUMMARY

Among the investigated samplers, we find no benefit to using gradient-based NFMC without tuning NF hyperparameters. Jump MH is better than all other gradient-free samplers, even without hyperparameter tuning. NeuTra HMC ranks worse than Jump HMC and is on par with HMC when tuned properly. NeuTra MH is also worse than Jump MH but better than MH when tuned properly. Having found contexts where NFMC is better than MCMC, we now evaluate different NF architectures to see which one yields the best NFMC performance.

4.2 NF architecture evaluation

In this section, we empirically compare NF architectures in various contexts and provide model choice guidelines. We give NF recommendations based on our findings at the end of this section.

4.2.1 JUMP PERFORMANCE ON DIFFERENT TARGET FAMILIES

We compare the performance of different NFs in Jump MCMC for different target families. We focus on experiments where NFs use their default hyperparameters. We show the results in Table 2.

All four affine and spline-based autoregressive NFs achieve $\bar{r} < 0$ on Gaussian targets. This is reasonable because NAF transformers have many more trainable parameters than are needed to model Gaussian distributions. C-RQ-NSF achieves the lowest \bar{r} of all NFs, making it the obvious default choice for approximately Gaussian targets. However, the conceptually similar C-LR-NSF ranks worse with greater uncertainty. We found that C-RQ-NSF yields $\bar{r} < -0.43$ on each Gaussian target, while results vary greatly for C-LR-NSF. It yields $\bar{r} = -1.59$ on the ill-conditioned full-rank Gaussian target and $\bar{r} = 1.59$ on the full-rank Gaussian target. The major difference is in the spline definition, which suggests that the LRS transformer is less stable than RQS, as both transformers use nearly identical spline parameterizations otherwise. Among residual NFs, i-ResNet is tied for the second-best NF on Gaussians, while ResFlow ranks noticeably worse. We further investigated the difference by narrowing the comparison to standard and diagonal Gaussian targets. We found i-ResNet to always achieve lower b^2 on both targets across all jump MCMC samplers. ResFlow wins

NF	Gaussian	Non-Gaussian	Multimodal	Real-world	All
NICE	-0.43 ± 0.31	1.45 ± 0.14	-0.80 ± 0.25	0.00 ± 0.32	-0.11 ± 0.22
Real NVP	-0.80 ± 0.25	-1.16 ± 0.43	0.29 ± 0.36	0.29 ± 0.32	-0.11 ± 0.22
C-LR-NSF	-0.14 ± 0.72	0.72 ± 0.58	-0.51 ± 0.30	-0.40 ± 0.19	-0.24 ± 0.20
C-RQ-NSF	-0.87 ± 0.19	1.01	-0.51 ± 0.38	0.43 ± 0.39	0.00 ± 0.24
C-NAF _{deep}	0.58 ± 0.19	-0.14 ± 0.87	0.72 ± 0.35	0.80 ± 0.25	0.63 ± 0.17
C-NAF _{dense}	0.94 ± 0.46	0.29 ± 0.14	0.58 ± 0.65	1.09 ± 0.15	0.85 ± 0.18
C-NAF _{both}	1.30 ± 0.20	0.29 ± 0.43	0.72 ± 0.78	0.76 ± 0.29	0.82 ± 0.22
i-ResNet	-0.80 ± 0.36	-0.14 ± 0.58	-0.07 ± 0.60	-0.98 ± 0.25	-0.64 ± 0.20
ResFlow	0.22 ± 0.62	-0.29 ± 0.14	0.80 ± 0.18	-0.18 ± 0.33	0.11 ± 0.21
CNF _{Euler}	0.14 ± 0.35	-0.87 ± 0.43	-0.36 ± 0.62	-0.54 ± 0.31	-0.39 ± 0.21
CNF _{RK}	0.29 ± 0.65	0.0 ± 1.6	-0.07 ± 0.48	-0.72 ± 0.27	-0.27 ± 0.26
CNF _{RK(R)}	-0.43 ± 0.31	-1.16 ± 0.14	-0.80 ± 0.27	-0.54 ± 0.32	-0.64 ± 0.17

Table 2: $\bar{r} \pm \hat{\sigma}$ for all NFs and target families in IMH, Jump MH, and Jump HMC. NFs in the top 20th percentile are shown in bold for each target family. We estimate $\bar{r} \pm \hat{\sigma}$ with b^2 from runs with default hyperparameters. Entries without $\hat{\sigma}$ always attain the same \bar{r} . Ranks are computed separately for each target family.

in four of six full-rank Gaussian experiments. This does not necessarily imply that one estimator is more suited for Gaussians than the other because i-ResNet parameterizes g with two hidden layers of size 10 by default, and ResFlow parameterizes it with five hidden layers of size 100 by default. However, i-ResNet is a better off-the-shelf architecture for diagonal Gaussians and a decent option for full-rank ones. CNF_{RK(R)} is the only continuous NF with $\bar{r} < 0$ on Gaussians. However, all continuous architectures exhibit a relatively high uncertainty. Their unrestricted Jacobian allows very expressive transformations. However, this is unnecessary on Gaussians, which only require an appropriate scale, rotation, and shift of the base standard Gaussian distribution.

CNF_{RK(R)}, Real NVP, and CNF_{Euler} rank best for non-Gaussian sampling. CNF_{RK(R)} is the preferred default choice due to having lower uncertainty than Real NVP. Furthermore, all NFs except CNF_{RK(R)} either attain a poor \bar{r} or a high uncertainty, making most methods ineffective with default hyperparameters. After checking specific experiment results, we found Real NVP to achieve the lowest b^2 across all three Jump MCMC samplers on the funnel target when using default hyperparameters. This is sensible because an exact transformation from standard Gaussian to the funnel involves scaling dimensions by multiplying them with the exponential function of the first dimension. The Real NVP architecture easily learns this transformation provided the first transformer is conditioned on the first dimension. NICE ranks the worst of all autoregressive NFs as it only transforms with a shift and only uses two bijective layers in its default hyperparameter set. Note that each coupling NF contained at least one coupling layer where the first dimension was passed to the conditioner. All coupling NFs except NICE could thus find an exact solution for the funnel. CNF_{RK(R)}, NICE, and both NSF models achieve the best \bar{r} on multimodal targets. All other methods again exhibit poor \bar{r} or high uncertainty. As NF families, residual and continuous NFs outperform autoregressive NFs on real-world Bayesian model posterior targets. i-ResNet ranks the best, followed by the three continuous architectures.

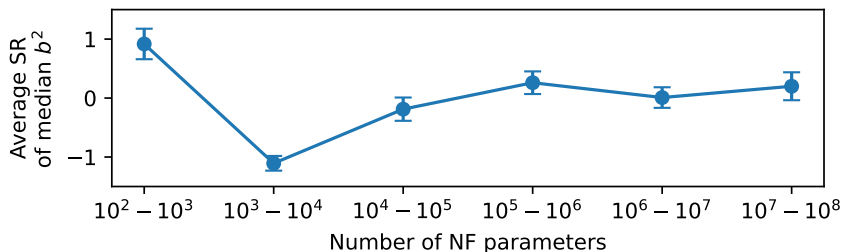


Figure 2: $\bar{r} \pm \hat{\sigma}$ for groups of NFs, defined using \log_{10} of the trainable NF parameter count. Groups were ranked for each target individually and then averaged across all targets.

The best-performing architectures across all targets are $\text{CNF}_{\text{RK(R)}}$, i-ResNet, and $\text{CNF}_{\text{Euler}}$. All obtain \bar{r} on each family except $\text{CNF}_{\text{Euler}}$ on Gaussians. $\text{CNF}_{\text{RK(R)}}$ achieves better overall \bar{r} than CNF_{RK} , suggesting that regularization is beneficial for continuous NF models. NAF models rank the worst, which could be due to having a very high parameter count. A high parameter count increases the space of possible solutions, which can result in slower training. Additionally, NAF models use neural network transformers, which are more difficult to optimize than affine or spline maps. Residual NFs and continuous NFs have fewer restrictions on the form of their bijections than autoregressive NFs. This could explain their better performance on real-world targets, whose complex geometry requires expressive bijections to be modeled. Having observed how the bijection form can contribute to sampling quality, we also investigate the effect of the NF parameter count. In Figure 2, we plot the trainable parameter count against the SR of the NF.

We find a noticeable improvement in performance with 10^3 to 10^4 parameters where we observe a dip in SR. The results verify our claim that one must choose hyperparameters that create a suitably expressive architecture. Furthermore, they suggest that NF parameter counts in this range are a suitable default choice. For SVI with Real NVP, Agrawal and Domke (2024) generally recommend using 10 or more for targets with complex geometry, as well as many hidden units for high-dimensional targets. Our analysis shows that these recommendations do not directly translate into NFMC, as the best results are generally achieved by NFs with few parameters.

Lastly, we provide a measure of jump efficiency for a chosen NF, independent of other architectures: we check the number of targets in our benchmark where IMH with a particular NF proposal achieves lower b^2 than MH and HMC. The former lets us measure jump efficiency in the gradient-free setting, while the latter measures gradient-based performance. For each target where IMH achieves lower b^2 , we know that independent jumps with NFs are a more efficient exploration strategy than MCMC. We show the results in Figure 3.

Regardless of which NF we choose, IMH is better than MH in at least 60% of all cases. The improvement is clear even when only considering the default NF hyperparameters. Independent jumps prove to be a much weaker exploration strategy compared to gradient-based HMC exploration. Continuous NFs beat HMC on 50% of all targets in the best case and are slightly worse when using default hyperparameters. We observe a similar pattern with residual NFs. The superior performance of continuous and residual NFs is consistent with their better ranks in Table 2. While independent jumps are a suitable

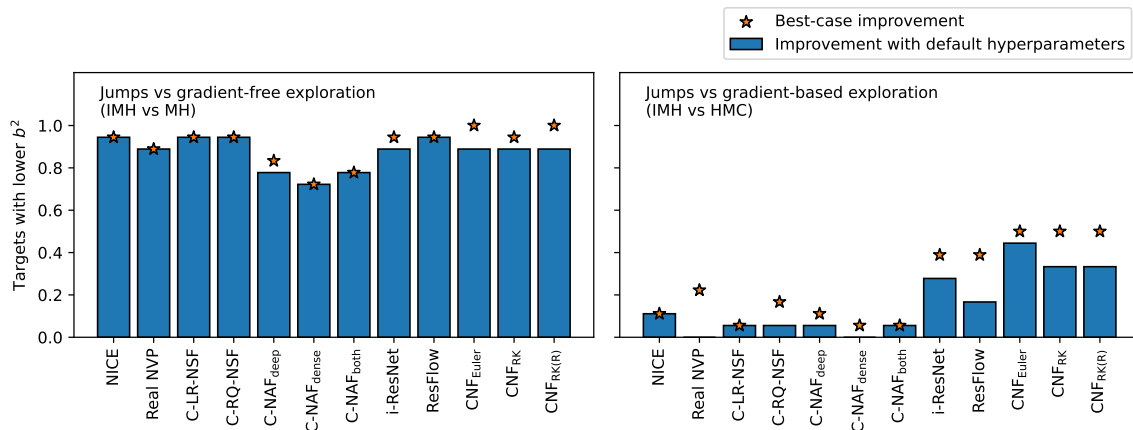


Figure 3: Jump efficiency for NF architectures with and without target log density gradients, measured by the fraction of benchmark targets where IMH yields smaller b^2 than MH (left) and HMC (right). Bars denote IMH performance with default NF hyperparameters and stars denote IMH performance, corresponding to the minimum b^2 across all hyperparameter sets for an experiment.

strategy for general gradient-free sampling, they are clearly inefficient for gradient-based targets if we have no prior knowledge. These results are also consistent with Table 1, where Jump MH outperforms MH and IMH, and Jump HMC outperforms HMC and IMH, further emphasizing the importance of mixing independent NF proposals with local MCMC exploration.

4.2.2 PRECONDITIONING QUALITY ON DIFFERENT TARGET FAMILIES

We compare NF architectures by their performance in NeuTra MCMC. Before interpreting the results, we note that NeuTra HMC performed much worse than regular HMC. Furthermore, while NeuTra MH improved upon regular MH, it was still vastly inferior to Jump MH. This means that NeuTra MCMC may not be a very efficient preconditioning method, and the best-performing NFs could favor those whose transformation is close to the identity map. We list the results in Table 3.

As groups, both IA and residual NFs perform the best across all targets (last column). This is unsurprising because IA and radial flows were designed to improve variational inference (Tabak and Turner, 2013; Rezende and Mohamed, 2015; Kingma et al., 2016), which forms the crucial NF warm-up phase in NeuTra MCMC. Interestingly, the radial flow performs better than IA within NeuTra MCMC despite the fact that IAF has been proposed to address the limitations of the former. NeuTra MCMC can benefit from simpler preconditioning of the radial flow, which does not use neural networks, compared to more expressive bijections. However, the form of the bijection could play a role, as the simple planar NF ranks worse than radial and Sylvester flows.

The radial flow reaches the top 20% of all NFs for every target family. The next best are ResFlow and IA-NAF_{deep}, which rank among the best in all but multimodal sampling. The radial flow appears somewhat more stable on real-world targets, while ResFlow is decisively

NF	Gaussian	Non-Gaussian	Multimodal	Real-world	All
NICE	0.21 ± 0.42	1.07 ± 0.25	0.62 ± 0.38	−0.31 ± 0.27	0.17 ± 0.20
Real NVP	0.17 ± 0.32	1.57 ± 0.08	0.83 ± 0.29	0.52 ± 0.37	0.62 ± 0.21
C-LR-NSF	−0.62 ± 0.42	0.33 ± 0.33	−0.37 ± 0.49	0.20 ± 0.32	−0.10 ± 0.21
C-RQ-NSF	−0.87 ± 0.33	0.33 ± 0.17	−0.04 ± 0.25	−0.45 ± 0.33	−0.36 ± 0.18
C-NAF _{deep}	1.07 ± 0.08	0.50 ± 0.17	1.40 ± 0.11	0.62 ± 0.41	0.88 ± 0.20
C-NAF _{dense}	0.33 ± 0.45	−0.91 ± 0.58	1.11 ± 0.23	0.56 ± 0.30	0.47 ± 0.22
C-NAF _{both}	0.04 ± 0.32	−0.99 ± 0.33	0.25 ± 0.29	0.08 ± 0.37	−0.02 ± 0.20
IAF	0.54 ± 0.44	1.16 ± 0.33	−0.04 ± 0.60	0.39 ± 0.27	0.41 ± 0.21
IA-LR-NSF	−0.25 ± 0.55	−0.25 ± 0.08	0.37 ± 0.62	−0.07 ± 0.41	−0.03 ± 0.25
IA-RQ-NSF	−0.62 ± 0.44	−0.50 ± 0.33	−0.87 ± 0.31	−0.30 ± 0.28	−0.52 ± 0.17
IA-NAF _{deep}	−0.83 ± 0.24	−1.16 ± 0.33	−0.37 ± 0.40	−0.45 ± 0.38	−0.59 ± 0.20
IA-NAF _{dense}	−0.54 ± 0.27	−0.91 ± 0.41	−0.87 ± 0.37	−0.26 ± 0.34	−0.53 ± 0.19
IA-NAF _{both}	0.29 ± 0.25	−0.58 ± 0.08	0.12 ± 0.46	−0.25 ± 0.38	−0.07 ± 0.20
i-ResNet	−0.58 ± 0.27	−0.58 ± 0.58	−0.70 ± 0.18	−0.39 ± 0.21	−0.52 ± 0.13
ResFlow	−0.95 ± 0.39	−1.07 ± 0.08	−0.62 ± 0.24	−0.43 ± 0.22	−0.66 ± 0.14
Planar	0.29 ± 0.55	0.25 ± 0.08	−0.04 ± 0.21	−0.11 ± 0.31	0.04 ± 0.18
Radial	−1.16 ± 0.39	−1.32 ± 0.33	−1.57 ± 0.08	−1.07 ± 0.21	−1.23 ± 0.13
Sylvester	−0.74 ± 0.20	−0.6 ± 1.1	0.00 ± 0.24	−0.67 ± 0.34	−0.47 ± 0.19
CNF _{Euler}	1.49	0.99	0.00 ± 0.58	0.58 ± 0.39	0.70 ± 0.24
CNF _{RK}	1.32 ± 0.23	1.49 ± 0.17	0.08 ± 0.86	0.93 ± 0.38	0.89 ± 0.27
CNF _{RK(R)}	1.40 ± 0.08	1.16	0.70 ± 0.57	0.37 ± 0.43	0.76 ± 0.24

Table 3: $\bar{r} \pm \hat{\sigma}$ for all NFs and target families in NeuTra MH and NeuTra HMC. NFs in the top 20th percentile are shown in bold for each target family. We estimate $\bar{r} \pm \hat{\sigma}$ with b^2 from runs with default hyperparameters. Entries without $\hat{\sigma}$ always attain the same \bar{r} . Ranks are computed separately for each target family.

stabler on synthetic targets. However, both attain the same uncertainty when evaluated across all targets. We also notice good performance in some architectures that do not fit this pattern, namely coupling NFs. While continuous NFs generally achieve better-than-average ranks on Jump MCMC, all of them perform poorly on NeuTra MCMC. We again notice that CNF_{RK(R)} achieves lower \bar{r} than CNF_{RK}, which is consistent with our findings in Jump MCMC and further shows the benefits of using regularization in continuous NFs.

Our results also shed light on Hoffman et al. (2019), who precondition HMC with the IAF bijection, which improves moment estimates over HMC on the funnel target. However, the second column of Table 3 shows that IAF is one of the worst-performing NFs for the funnel and Rosenbrock distributions. The discrepancy could be due to differences in implementation, namely the number of chains: they use 16384 parallel chains on the GPU, whereas we use 100 on the CPU. We cannot afford such a big number of GPU chains, as it would require a prohibitive amount of computational resources for a fair comparison with other, usually slower NFs. Hoffman et al. (2019) also use a bigger SVI batch size compared to our single-sample unbiased loss estimator, which could contribute to good results. We consider their IAF results complementary to ours, where we work with moderate computational resources, and they consider the case of higher resource and power consumption. We also comment on batch size choices in Appendix B.3.

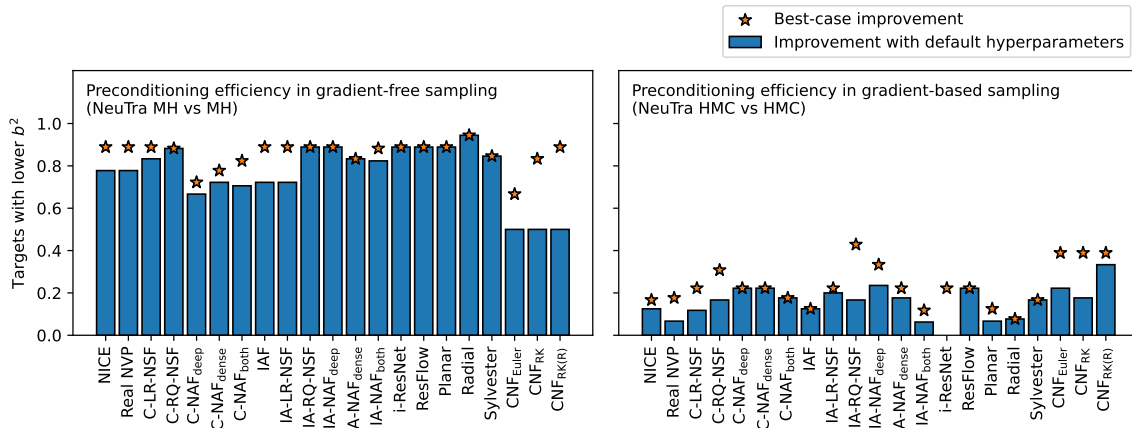


Figure 4: Preconditioning efficiency for investigated NF architectures with and without target log density gradients, measured by the fraction of benchmark targets where NeuTra MCMC yields smaller b^2 than MCMC. Bars denote NeuTra MCMC performance with default NF hyperparameters, and stars denote NeuTra MCMC performance, corresponding to the minimum b^2 across all hyperparameter sets for an experiment.

As before, we provide a measure of preconditioning efficiency for a particular NF, independent of other architectures. For gradient-free sampling, we observe the percentage of targets where NeuTra MH achieves lower b^2 than MH. We compare NeuTra HMC to HMC in the same way for gradient-based sampling. We show the results in Figure 4.

NeuTra MCMC shows the biggest improvement in the gradient-free case. Continuous NFs have the worst gradient-free preconditioning performance with default hyperparameters, which is consistent with Table 3. However, they roughly match the performance of other NFs if tuned properly. NeuTra MCMC is inefficient across the board in the gradient-based case, and improvements remain relatively small after hyperparameter tuning. This matches with the best-case results in Table 1, where NeuTra HMC performs worse than Jump HMC and is similar to HMC. CNF_{RK(R)} performs better in NeuTra HMC relative to other architectures than in NeuTra MH, despite attaining a poor average SR in Table 3. Conversely, the radial flow improves on fewer targets relative to other architectures in gradient-based sampling despite ranking the best in NeuTra MCMC. This suggests that the choice of sampler plays a role in preconditioning efficiency. However, gradient-based NF preconditioning is still an ineffective sampling strategy for our benchmark.

4.2.3 VARYING PROPERTIES OF SYNTHETIC TARGETS

In this section, we investigate the performance of NF architectures when different properties of synthetic distributions vary: dimensionality, curvature strength, number of multimodal components, and weights of multimodal components. On the one hand, this lets us compare NFs on challenging target distributions with high dimensionality, high multimodality, and strong curvature. On the other, we attain a measure of NF scalability in terms of these properties.

NF	Dimensionality	Curvature	Mode weight	Components	All
NICE	-0.68 ± 0.24	-0.48 ± 0.27	-0.26 ± 0.19	-0.34 ± 0.23	-0.43 ± 0.11
Real NVP	-0.13 ± 0.24	-0.41 ± 0.28	-0.06 ± 0.17	-0.18 ± 0.23	-0.18 ± 0.11
C-LR-NSF	-0.27 ± 0.17	-1.01 ± 0.14	-0.45 ± 0.27	-0.34 ± 0.19	-0.49 ± 0.11
C-RQ-NSF	-0.68 ± 0.21	-0.39 ± 0.17	-0.31 ± 0.18	-0.49 ± 0.21	-0.46 ± 0.10
C-NAF _{deep}	0.55 ± 0.23	0.29 ± 0.31	0.50 ± 0.21	0.43 ± 0.26	0.45 ± 0.12
C-NAF _{dense}	0.64 ± 0.25	0.68 ± 0.25	0.43 ± 0.16	0.40 ± 0.19	0.52 ± 0.10
C-NAF _{both}	0.70 ± 0.26	0.80 ± 0.32	1.24 ± 0.13	0.74 ± 0.28	0.90 ± 0.12
i-ResNet	-0.21 ± 0.19	0.10 ± 0.15	-0.06 ± 0.18	0.20 ± 0.27	0.00 ± 0.10
ResFlow	-0.37 ± 0.21	0.19 ± 0.23	-0.18 ± 0.18	0.07 ± 0.25	-0.09 ± 0.11
CNF _{Euler}	0.30 ± 0.28	0.36 ± 0.27	-0.39 ± 0.32	-0.09 ± 0.27	0.01 ± 0.15
CNF _{RK}	0.33 ± 0.29	0.00 ± 0.26	-0.03 ± 0.23	-0.03 ± 0.25	0.07 ± 0.13
CNF _{RK(R)}	0.02 ± 0.29	-0.12 ± 0.38	-0.43 ± 0.27	-0.38 ± 0.32	-0.24 ± 0.15

Table 4: $\bar{r} \pm \hat{\sigma}$ for NFs in Jump MCMC given NF scalability scores when varying target properties: dimensionality, curvature strength, variance of mode weights, number of modes. NFs with \bar{r} in the 20th percentile are shown in bold. Ranks computed separately for each target property.

For scalability with dimensionality, we consider a diagonal Gaussian target with 2, 10, 100, 1000, and 10.000 dimensions. For increasing curvature strength, we consider a 100D funnel target with first dimension scales equal to 0.01, 0.1, 1, 10, and 100. For uneven multimodal weight tests, we consider the 20-component 100D Gaussian mixture with scales $\lambda \in \{0, 1, 2, 3, 4, 5\}$ and weight of component i equal to $w_i = \text{softmax}(\lambda u)_i$, where $u_i \sim_{iid} N(0, 1)$. Scale $\lambda = 0$ results in equal weights. For the increasing number of components, we consider both mixtures from Section 3.3.1 with 2, 8, 32, 128, and 512 components. For each experiment, we first compute the median b^2 across NFMC methods and varied experiment values for each NF, then \bar{r} and $\hat{\sigma}$ according to these medians. We first report the results for Jump MCMC experiments in Table 4.

Aside from NAF, we find that autoregressive architectures generally outperform both residual and continuous NFs, always achieving $\bar{r} < 0$. NICE and the two NSF architectures rank the best overall, followed by CNF_{RK(R)}. This puts into perspective the previous results from Table 2: continuous NFs performed much better on the basic benchmark, but they rank worse when increasing the complexity of synthetic targets.

We also report experiment results for NeuTra MCMC in Table 5. C-LR-NSF handles complex synthetic targets the best, followed by inverse autoregressive NFs and contractive residual NFs. C-LR-NSF, IA-NAF_{deep}, i-ResNet, and ResFlow always attain $\bar{r} < 0$, IA-NAF models perform better than their coupling counterparts despite both having a large number of transformer parameters. This suggests that MADE conditioners are better suited for NAF transformers in NeuTra MCMC, which is also consistent with Jump MCMC results from Table 3. Despite its good performance on the regular benchmark, the radial flow is the worst overall for these synthetic target variations. The poor ranks of continuous NF models are consistent with their poor NeuTra MCMC results on the regular benchmark.

NF	Dimensionality	Curvature	Mode weight	Components	All
NICE	0.01 ± 0.14	-0.38 ± 0.33	-0.93 ± 0.15	-0.42 ± 0.31	-0.46 ± 0.13
Real NVP	0.05 ± 0.22	-0.85 ± 0.26	-0.62 ± 0.21	0.10 ± 0.22	-0.32 ± 0.13
C-LR-NSF	-0.60 ± 0.14	-0.44 ± 0.38	-1.16 ± 0.10	-0.47 ± 0.30	-0.70 ± 0.12
C-RQ-NSF	0.29 ± 0.17	-0.74 ± 0.53	-1.27 ± 0.11	-0.39 ± 0.30	-0.53 ± 0.15
C-NAF _{deep}	0.38 ± 0.43	0.87 ± 0.25	1.12 ± 0.07	0.50 ± 0.35	0.73 ± 0.15
C-NAF _{dense}	0.33 ± 0.51	0.60 ± 0.27	0.59 ± 0.08	0.19 ± 0.31	0.43 ± 0.14
C-NAF _{both}	0.47 ± 0.50	0.47 ± 0.33	0.51 ± 0.07	0.24 ± 0.26	0.42 ± 0.13
IAF	0.50 ± 0.25	0.03 ± 0.30	-1.11 ± 0.10	-0.44 ± 0.31	-0.31 ± 0.15
IA-LR-NSF	-0.06 ± 0.19	0.10 ± 0.14	-0.65 ± 0.13	-0.88 ± 0.24	-0.41 ± 0.11
IA-RQ-NSF	-0.06 ± 0.28	0.00 ± 0.24	-0.93 ± 0.11	-0.67 ± 0.32	-0.51 ± 0.14
IA-NAF _{deep}	-0.16 ± 0.20	-0.05 ± 0.44	-0.83 ± 0.18	-0.84 ± 0.20	-0.51 ± 0.13
IA-NAF _{dense}	-0.53 ± 0.34	-0.08 ± 0.26	0.34 ± 0.22	0.48 ± 0.18	0.09 ± 0.14
IA-NAF _{both}	-0.51 ± 0.40	-0.05 ± 0.25	0.80 ± 0.20	0.53 ± 0.20	0.27 ± 0.15
i-ResNet	-0.30 ± 0.40	-0.83 ± 0.41	-0.33 ± 0.12	-0.59 ± 0.22	-0.47 ± 0.16
ResFlow	-0.38 ± 0.23	-1.32 ± 0.28	-0.33 ± 0.15	-0.03 ± 0.26	-0.44 ± 0.14
Planar	0.43 ± 0.19	-0.64 ± 0.19	-0.02 ± 0.14	-0.19 ± 0.22	-0.07 ± 0.10
Radial	-0.11 ± 0.51	0.89 ± 0.46	1.65	1.65	1.12 ± 0.18
Sylvester	-0.40 ± 0.15	-0.31 ± 0.44	-0.16 ± 0.08	-0.32 ± 0.23	-0.29 ± 0.11
CNF _{Euler}	0.28 ± 0.45	0.65 ± 0.33	1.19 ± 0.09	0.27 ± 0.39	0.62 ± 0.17
CNF _{RK}	0.98 ± 0.30	0.70 ± 0.28	0.90 ± 0.24	0.72 ± 0.35	0.83 ± 0.14
CNF _{RK(R)}	-0.82 ± 0.35	-0.07 ± 0.30	0.92 ± 0.05	0.24 ± 0.21	0.12 ± 0.15

Table 5: $\bar{\tau} \pm \hat{\sigma}$ for NFs in NeuTra MCMC given NF scalability scores when varying target properties: dimensionality, curvature strength, variance of mode weights, number of modes. NFs with $\bar{\tau}$ in the 20th percentile are shown in bold. Ranks computed separately for each target property.

4.2.4 MEASURING NF STABILITY VIA HYPERPARAMETER SENSITIVITY

We have observed several times that certain NF architectures exhibit a high standard error $\hat{\sigma}$ when estimating $\bar{\tau}$. This partly depends on the variance of b^2 when testing the same architecture with multiple hyperparameter sets or different samplers. If the variance is high, we expect the architecture to be sensitive to hyperparameter choice and thus require more time for hyperparameter tuning. While our previous tests measured NF performance on our regular benchmark, we now further test NF stability when varying properties of synthetic distributions to make sampling more challenging. We expect stable NFs to exhibit a low variance of b^2 across multiple different hyperparameter sets and samplers. We separately rank NFs across all benchmark targets in terms of $\text{Var}[b^2]$ in Figure 5.

We find NF stability to be roughly the same in Jump MH and Jump HMC experiments. Coupling NFs are the most stable architectures in Jump MH. They rank somewhat worse in Jump HMC, where residual NFs perform better. Continuous NFs are the least stable in both Jump MH and Jump HMC. However, they are the best option for IMH, suggesting that they gain stability if we remove local MCMC transitions. Conversely, coupling NFs lose stability if we add local transitions.

IA architectures rank the best in NeuTra MH, closely followed by i-ResNet and ResFlow. The latter two are substantially better in NeuTra HMC, which is also consistent with

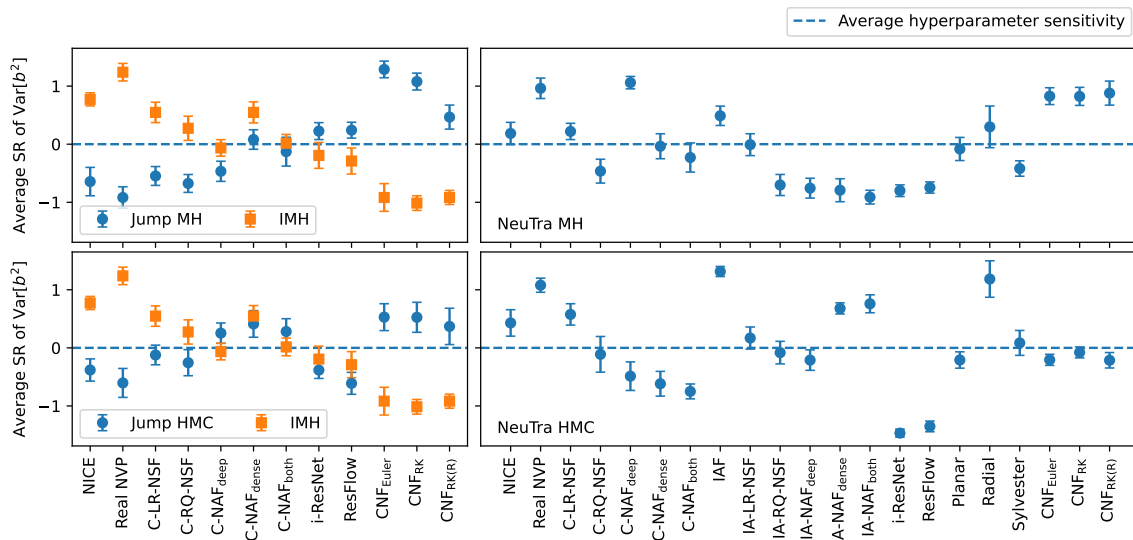


Figure 5: Hyperparameter sensitivity for different NFs across all benchmark targets for Jump MCMC (left) and NeuTra MCMC (right), described as $\bar{r} \pm \hat{\sigma}$ where NFs are ranked according to $\text{Var}[b^2]$ across all hyperparameter configurations.

their improved stability after switching from Jump MH to Jump HMC. The most stable NeuTra HMC preconditioners are C-NAF architectures, i-ResNet, and ResFlow. The radial flow is among the least stable ones. Combined with our findings in Table 3, its good performance is thus highly dependent on the choice of hyperparameters. IAF is the least stable preconditioner for NeuTra HMC, further suggesting that the original NeuTra HMC formulation in (Hoffman et al., 2019) can easily be improved for general-purpose sampling with a different architecture like i-ResNet or ResFlow.

4.2.5 NF RECOMMENDATIONS FOR NFMC

Practitioners interested in performing statistical analyses of models or distributions of their parameters are usually focused on obtaining the best quality samples and parameter estimates. Considering our classification of distributions into four target families, we state the following:

- If the practitioner has no knowledge of the target family and this knowledge is unattainable, we recommend Jump HMC with i-ResNet due to its good sampling performance and hyperparameter stability. One may also use other continuous or residual architectures. If the target has high dimensionality, curvature, or multimodality, we recommend coupling NFs instead (excluding NAF models). We also recommend such NFs over continuous NFs to reduce tuning time, as coupling NFs are less sensitive to the choice of hyperparameters in Jump MCMC.
- If the practitioner has knowledge of the target family, we recommend Jump HMC with C-RQ-NSF for approximately Gaussian targets, $\text{CNF}_{\text{RK(R)}}$ or Real NVP for unimodal non-Gaussian targets, and either $\text{CNF}_{\text{RK(R)}}$ or NICE for multimodal targets.

If dealing with a general (real-world) Bayesian model posterior, we suggest i-ResNet or a continuous NF architecture.

Researchers can also be interested in NF performance to guide the design and development of new NFMC samplers:

- If using NFs for jumps as independent global proposals, we suggest continuous NFs in both gradient-free and gradient-based cases as they offer the best gradient-based performance with or without hyperparameter tuning. However, we again note that continuous NFs may prove to be sensitive across hyperparameters depending on the underlying MCMC dynamics. A stabler option is coupling NFs (excluding NAF).
- If using NFs for preconditioning, we suggest the radial flow with default hyperparameters, contractive residual NFs, and IA architectures. If the target distribution has high dimensionality, strong curvature, many modes, or heavily unequal mode weights, one may opt for coupling NFs (excluding NAF). For a lower hyperparameter sensitivity, we suggest IA architectures in the gradient-free setting and contractive residual NFs in the gradient-based setting.

For target distributions similar to the ones in our benchmark, we suggest keeping NF parameter counts between roughly 10^3 and 10^4 , especially if moment estimates with bigger or lower trainable parameter counts are poor.

5 Conclusion

In this paper, we compared different NFMC methods and NF architectures in sampling from distributions. We focused on the quality of second-moment estimation and tested many NFMC-NF combinations on various targets across four distribution families. We focused on variations of HMC and MH as gradient-based and gradient-free MCMC representatives, extending them with independent NF jumps and NF-based preconditioning. When comparing MCMC to NFMC with off-the-shelf hyperparameters, we found HMC to perform better than NeuTra HMC and comparable to Jump HMC. IMH, Jump MH, and NeuTra MH all outperformed MH. When picking the best NF architecture and hyperparameters for a particular target, we found Jump HMC to outperform all other samplers. IMH, Jump MH, and NeuTra MH all outperformed MH. In summary, we found jumps beneficial in all cases and preconditioning useful for gradient-free sampling. We found i-ResNet to generally be the best architecture for NFMC on our benchmark, followed by other residual NFs. NFMC samplers should consider such NFs as candidates, especially since many previously proposed samplers perform NF jumps or preconditioning with Real NVP and NSF models. Aside from NAF, we found coupling NFs to attain relatively average results. However, they were the most robust when the geometric complexity of the target was increased. We found the radial flow to rank best in NeuTra MCMC with default hyperparameters. However, it was very sensitive to hyperparameter choice and performed poorly on complex synthetic targets.

Given our findings, it would be practical to re-evaluate and compare other NFMC samplers (Grumitt et al., 2022; Cabezas and Nemeth, 2023; Williams et al., 2021), as well as transport methods (Karamanis et al., 2022; Grumitt et al., 2024; Wu et al., 2020; Arbel et al., 2021; Matthews et al., 2022) with the best architectures for the corresponding target families. We similarly suggest using the highlighted NFs for the development of

future samplers or as methods to be extended into NFMC-specific NF architectures. Our results also suggest evaluating current and future NFMC samplers across various targets and, importantly, comparing them with classic MCMC methods to assess their practical uses.

5.1 Limitations

Our focus was on evaluating and comparing NF architectures within NFMC, which we performed with extensions of MH and HMC. Due to a combinatorial explosion of the number of possible experiments, we did not analyze other MCMC and NFMC samplers. Doing so could let us exhaustively compare different NFMC samplers, which would be highly relevant to the development of the field. We opted to first compare NFs, so we leave an exhaustive comparison of NFMC methods as future work. In our results, we sometimes estimate uncertainties based on a small number of distributions belonging to a target family. By adding more targets, we could arrive at better rank estimates and smaller standard errors.

Our results are based on over 10 thousand experiments. We paid careful attention to successfully execute each experiment. However, some experiments with specific combinations of samplers, NFs, and targets were not completed successfully. While rare, this was mostly due to the slow optimization of NFs with many trainable parameters, which occurred in high dimensional targets where we adaptively increased the NF parameter count to enable expressive modeling. Some experiments failed due to numerical instabilities in sampling from ill-posed targets or those stemming from sampler and NF definitions. We mitigated these issues by performing over 10 thousand automated tests for the numerical stability of samplers and NFs (forward and inverse passes, log probability computation, NF and MCMC sampling, and autodifferentiation).

We performed our experiments in PyTorch (Paszke et al., 2019). Several works show that using packages with just-in-time compilation, like Jax (Bradbury et al., 2018), can vastly speed up program execution. We opted for PyTorch as its object-oriented development paradigm allowed us to modularly implement and test each model. With Jax, managing such a large code base would require substantially more engineering effort. However, its faster execution speed could somewhat change the relative ranks of NFs and NFMC samplers in our results. Nevertheless, our results show that some combinations of NFs and NFMC methods consistently yield better results than others. Having identified these combinations, future research in NFMC can take them as initial models, refine and tune them according to their own target distribution needs, and finally implement them in Jax for maximum performance.

5.2 Software

We developed several new packages for our experiments. All code is publicly available:

- Normalizing flow implementations: <https://github.com/davidnabergoj/torchflows>.
- Sampler implementations: <https://github.com/davidnabergoj/nfmc>.
- Target distribution benchmark: <https://github.com/davidnabergoj/potentials>.
- Evaluation scripts: <https://github.com/davidnabergoj/nfmc-nf-evaluation>.

Acknowledgments and Disclosure of Funding

This work was supported by the Slovenian Research and Innovation Agency (ARIS) grant P2-0442.

References

- Ryan Abbott, Michael S. Albergo, Aleksandar Botev, Denis Boyda, Kyle Cranmer, Daniel C. Hackett, Alexander G. D. G. Matthews, Sébastien Racanière, Ali Razavi, Danilo J. Rezende, Fernando Romero-López, Phiala E. Shanahan, and Julian M. Urban. Aspects of scaling and scalability for flow-based sampling of lattice QCD. *The European Physical Journal A*, 59(11):257, 2023.
- Abhinav Agrawal and Justin Domke. Disentangling impact of capacity, objective, batchsize, estimators, and step-size on flow VI, 2024. arXiv:2412.08824.
- M. S. Albergo, G. Kanwar, and P. E. Shanahan. Flow-based generative models for Markov chain Monte Carlo in lattice field theory. *Physical Review D*, 100(3):034515, 2019.
- Michael Arbel, Alex Matthews, and Arnaud Doucet. Annealed Flow Transport Monte Carlo. In *Proceedings of the 38th International Conference on Machine Learning*, volume 139 of *Proceedings of Machine Learning Research*, pages 318–330. PMLR, 2021.
- Jens Behrmann, Will Grathwohl, Ricky T. Q. Chen, David Duvenaud, and Joern-Henrik Jacobsen. Invertible Residual Networks. In *Proceedings of the 36th International Conference on Machine Learning*, volume 97 of *Proceedings of Machine Learning Research*, pages 573–582. PMLR, 2019.
- Rianne van den Berg, Leonard Hasenclever, Jakub M. Tomczak, and M. Welling. Sylvester Normalizing Flows for Variational Inference. In *Proceedings of the 34th Conference on Uncertainty in Artificial Intelligence*, pages 393–402. AUAI Press, 2018.
- James Bradbury, Roy Frostig, Peter Hawkins, Matthew James Johnson, Chris Leary, Dougal Maclaurin, George Necula, Adam Paszke, Jake VanderPlas, Skye Wanderman-Milne, and Qiao Zhang. JAX: composable transformations of Python+NumPy programs, 2018. URL <http://github.com/google/jax>.
- James Brofos, Marylou Gabrié, Marcus A. Brubaker, and Roy R. Lederman. Adaptation of the Independent Metropolis-Hastings Sampler with Normalizing Flow Proposals. In *Proceedings of The 25th International Conference on Artificial Intelligence and Statistics*, volume 151 of *Proceedings of Machine Learning Research*, pages 5949–5986. PMLR, 2022.
- Alberto Cabezas and Christopher Nemeth. Transport Elliptical Slice Sampling. In *Proceedings of The 26th International Conference on Artificial Intelligence and Statistics*, volume 206 of *Proceedings of Machine Learning Research*, pages 3664–3676. PMLR, 2023.
- Ricky T. Q. Chen, Jens Behrmann, David K Duvenaud, and Joern-Henrik Jacobsen. Residual Flows for Invertible Generative Modeling. In *Advances in Neural Information Processing Systems*, volume 32. Curran Associates, Inc., 2019.

- Luigi Del Debbio, Joe Marsh Rossney, and Michael Wilson. Efficient Modelling of Trivializing Maps for Lattice ϕ^4 Theory Using Normalizing Flows: A First Look at Scalability. *Physical Review D*, 104(9):094507, 2021.
- Laurent Dinh, David Krueger, and Yoshua Bengio. NICE: Non-linear Independent Components Estimation, 2015. arXiv:1410.8516.
- Laurent Dinh, Jascha Sohl-Dickstein, and Samy Bengio. Density estimation using Real NVP, 2017. arXiv:1605.08803.
- Hadi Mohaghegh Dolatabadi, Sarah Erfani, and Christopher Leckie. Invertible Generative Modeling using Linear Rational Splines. In *Proceedings of The 23rd International Conference on Artificial Intelligence and Statistics*, volume 108 of *Proceedings of Machine Learning Research*, pages 4236–4246. PMLR, 2020.
- Felix Draxler, Stefan Wahl, Christoph Schnoerr, and Ullrich Koethe. On the Universality of Volume-Preserving and Coupling-Based Normalizing Flows. In *Proceedings of the 41st International Conference on Machine Learning*, volume 235 of *Proceedings of Machine Learning Research*, pages 11613–11641. PMLR, 2024.
- Conor Durkan, Artur Bekasov, Iain Murray, and George Papamakarios. Neural Spline Flows. In *Advances in Neural Information Processing Systems*, volume 32. Curran Associates, Inc., 2019.
- Chris Finlay, Joern-Henrik Jacobsen, Levon Nurbekyan, and Adam Oberman. How to Train Your Neural ODE: the World of Jacobian and Kinetic Regularization. In *Proceedings of the 37th International Conference on Machine Learning*, volume 119 of *Proceedings of Machine Learning Research*, pages 3154–3164. PMLR, 2020.
- Mathieu Germain, Karol Gregor, Iain Murray, and Hugo Larochelle. MADE: Masked Autoencoder for Distribution Estimation. In *Proceedings of the 32nd International Conference on Machine Learning*, volume 37 of *Proceedings of Machine Learning Research*, pages 881–889. PMLR, 2015.
- Will Grathwohl, Ricky T. Q. Chen, Jesse Bettencourt, Ilya Sutskever, and David Duvenaud. FFFJORD: Free-form Continuous Dynamics for Scalable Reversible Generative Models, 2018. arXiv:1810.01367.
- Louis Grenioux, Alain Oliviero Durmus, Éric Moulines, and Marylou Gabrié. On sampling with approximate transport maps. In *Proceedings of the 40th International Conference on Machine Learning*, volume 202 of *Proceedings of Machine Learning Research*, pages 11698–11733. PMLR, 2023.
- Richard Grumitt, Biwei Dai, and Uros Seljak. Deterministic Langevin Monte Carlo with Normalizing Flows for Bayesian Inference. In *Advances in Neural Information Processing Systems*, volume 35, pages 11629–11641. Curran Associates, Inc., 2022.
- Richard D. P. Grumitt, Minas Karamanis, and Uroš Seljak. Flow Annealed Kalman Inversion for Gradient-Free Inference in Bayesian Inverse Problems. *Physical Sciences Forum*, 9(1):21, 2024.

- Matthew D. Hoffman and Andrew Gelman. The No-U-Turn Sampler: Adaptively Setting Path Lengths in Hamiltonian Monte Carlo, 2011. arXiv:1111.4246.
- Matthew D. Hoffman, Pavel Sountsov, Joshua V. Dillon, Ian Langmore, Dustin Tran, and Srinivas Vasudevan. NeuTra-lizing Bad Geometry in Hamiltonian Monte Carlo Using Neural Transport, 2019. arXiv:1903.03704.
- Chin-Wei Huang, David Krueger, Alexandre Lacoste, and Aaron Courville. Neural Autoregressive Flows. In *Proceedings of the 35th International Conference on Machine Learning*, volume 80 of *Proceedings of Machine Learning Research*, pages 2078–2087. PMLR, 2018.
- M.F. Hutchinson. A stochastic estimator of the trace of the influence matrix for Laplacian smoothing splines. *Communication in Statistics – Simulation and Computation*, 18:1059–1076, 1989.
- Minas Karamanis, Florian Beutler, John A. Peacock, David Nabergoj, and Uroš Seljak. Accelerating astronomical and cosmological inference with preconditioned Monte Carlo. *Monthly Notices of the Royal Astronomical Society*, 516(2):1644–1653, 2022. Oxford University Press.
- Durk P Kingma, Tim Salimans, Rafal Jozefowicz, Xi Chen, Ilya Sutskever, and Max Welling. Improved Variational Inference with Inverse Autoregressive Flow. In *Advances in Neural Information Processing Systems*, volume 29. Curran Associates, Inc., 2016.
- Holden Lee, Chirag Pabbaraju, Anish Prasad Sevekari, and Andrej Risteski. Universal Approximation Using Well-Conditioned Normalizing Flows. In *Advances in Neural Information Processing Systems*, volume 34, pages 12700–12711. Curran Associates, Inc., 2021.
- Måns Magnusson, Jakob Torgander, Paul-Christian Bürkner, Lu Zhang, Bob Carpenter, and Aki Vehtari. posteriordb: Testing, Benchmarking and Developing Bayesian Inference Algorithms, 2024. arXiv:2407.04967.
- Alexander G. D. G. Matthews, Michael Arbel, Danilo J. Rezende, and Arnaud Doucet. Continual Repeated Annealed Flow Transport Monte Carlo. In *Proceedings of the 39th International Conference on Machine Learning*, volume 162 of *Proceedings of Machine Learning Research*, pages 15196–15219. PMLR, 2022.
- Laurence I. Midgley, Vincent Stimper, Gregor N. C. Simm, Bernhard Schölkopf, and Jose Miguel Hernandez-Lobato. Flow Annealed Importance Sampling Bootstrap. In *The Eleventh International Conference on Learning Representations*, 2023.
- George Papamakarios, Theo Pavlakou, and Iain Murray. Masked autoregressive flow for density estimation. In *Advances in Neural Information Processing Systems*, volume 30. Curran Associates, Inc., 2017.
- George Papamakarios, Eric Nalisnick, Danilo Jimenez Rezende, Shakir Mohamed, and Balaji Lakshminarayanan. Normalizing flows for probabilistic modeling and inference. *The Journal of Machine Learning Research*, 22(57):1–64, 2021.

- Adam Paszke, Sam Gross, Francisco Massa, Adam Lerer, James Bradbury, Gregory Chanan, Trevor Killeen, Zeming Lin, Natalia Gimelshein, Luca Antiga, Alban Desmaison, Andreas Köpf, Edward Yang, Zach DeVito, Martin Raison, Alykhan Tejani, Sasank Chilamkurthy, Benoit Steiner, Lu Fang, Junjie Bai, and Soumith Chintala. PyTorch: an imperative style, high-performance deep learning library. In *Advances in Neural Information Processing Systems*, volume 32, pages 8026–8037. Curran Associates Inc., 2019.
- Danilo Rezende and Shakir Mohamed. Variational Inference with Normalizing Flows. In *Proceedings of the 32nd International Conference on Machine Learning*, volume 37 of *Proceedings of Machine Learning Research*, pages 1530–1538. PMLR, 2015.
- Hadi Salman, Payman Yadollahpour, Tom Fletcher, and Kayhan Batmanghelich. Deep Diffeomorphic Normalizing Flows, 2018. arXiv:1810.03256.
- Sergey Samsonov, Evgeny Lagutin, Marylou Gabri e, Alain Durmus, Alexey Naumov, and Eric Moulines. Local-global MCMC kernels: the best of both worlds. In *Advances in Neural Information Processing Systems*, volume 37, pages 5178–5193. Curran Associates Inc., 2024.
- Samuel S. Schoenholz and Ekin D. Cubuk. JAX, M.D. A framework for differentiable physics. *Journal of Statistical Mechanics: Theory and Experiment*, 2021(12):124016, 2021.
- E. G. Tabak and Cristina V. Turner. A Family of Nonparametric Density Estimation Algorithms. *Communications on Pure and Applied Mathematics*, 66(2):145–164, 2013.
- Juli an Urbano, Harley Lima, and Alan Hanjalic. A New Perspective on Score Standardization. In *Proceedings of the 42nd International ACM SIGIR Conference on Research and Development in Information Retrieval*, pages 1061–1064. Association for Computing Machinery, 2019.
- Michael J. Williams, John Veitch, and Chris Messenger. Nested Sampling with Normalising Flows for Gravitational-Wave Inference. *Physical Review D*, 103(10):103006, 2021.
- Hao Wu, Jonas K ohler, and Frank Noe. Stochastic Normalizing Flows. In *Advances in Neural Information Processing Systems*, volume 33, pages 5933–5944. Curran Associates, Inc., 2020.

Appendix A. Additional results

In this section, we discuss additional results regarding NF operation speeds, autoregressive NF components, and experiments with a smaller time budget.

A.1 NF operation speed for moderate dimensional targets

Executing NF operations on the GPU can be much faster than the CPU when target dimensionality is high, such as for distributions of images. Such NFs consist of convolutional neural networks whose operations can be efficiently parallelized on the GPU. However, many analyses are performed on statistical models with fewer parameters and often on consumer-grade laptops. In such cases, it is practical to know whether GPUs are necessary for efficient NF operations or if CPUs suffice. In Figure 6, we compare the efficiency of GPU and CPU for three essential NF operations: computing the log probability of data points, sampling new data points, and computing the gradient of the loss. We use an AMD Ryzen 9 3900X 12-core CPU at 3.8 GHz and an NVIDIA RTX 2080S GPU in these experiments.

We find that MA and IA architectures are faster on the GPU for all operations. Out of the three autoregressive families, coupling NFs are the fastest on the CPU. Moreover, coupling NFs are faster on the CPU than the GPU for 64 or fewer dimensions. In continuous NFs and both residual NF families, we find that GPU operations are generally slower than CPU operations. Our results have practical relevance to the further development of general-purpose MCMC packages, as we find that the CPU is sufficient for key NF operations. This means practitioners and researchers can leverage NFMC for analyses with minimal hardware. Our findings are also promising for embedded systems without GPU support. We note that we perform autodifferentiation in an eager execution framework, and further work is needed to evaluate gradient computation speeds in graph execution configurations.

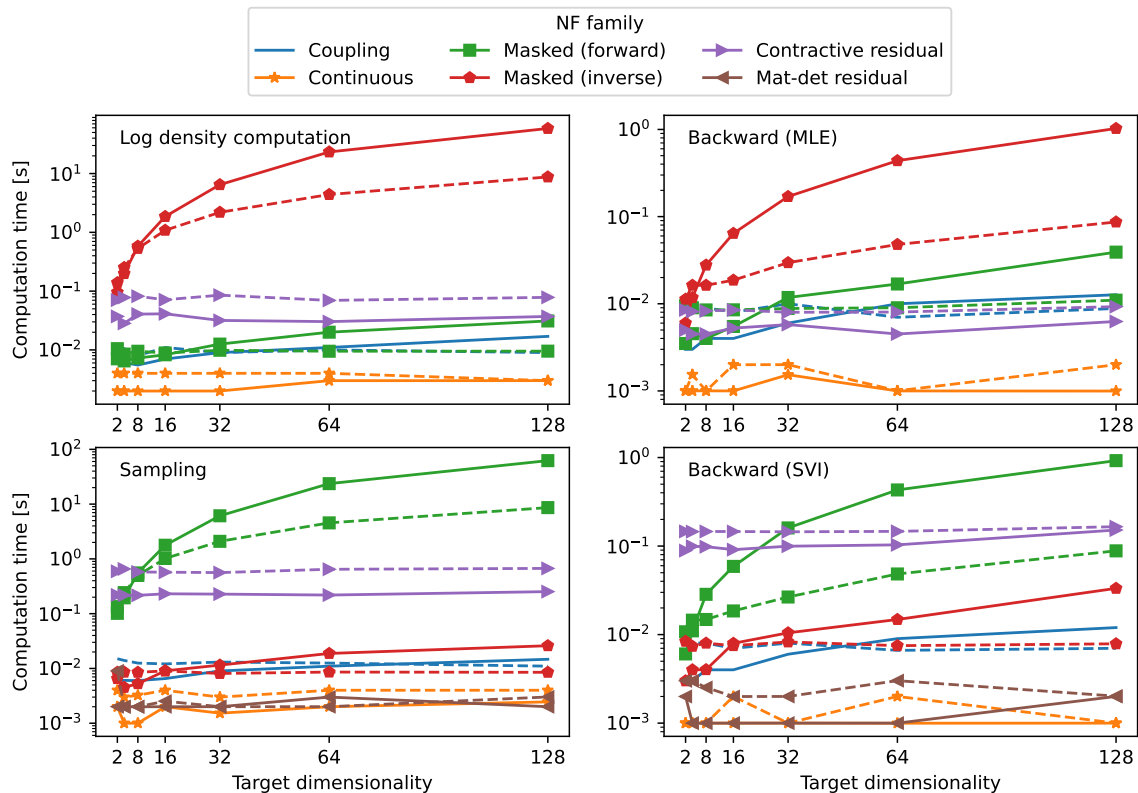


Figure 6: Computation time in seconds for density evaluation, sampling, and model parameter gradient computation via automatic differentiation (backward). Solid lines denote operations on the CPU, and dashed lines are operations on the GPU. Shown values are medians across operation times for NFs belonging to corresponding families. Operation times are averages of 100 trials with a hundred standard Gaussian vectors in 100D for each operation.

A.2 Autoregressive conditioner and transformer comparison in NeuTra MCMC

We compare different combinations of autoregressive conditioners (MADE and coupling) and transformers (affine maps, splines, and neural networks) in terms of moment estimation quality. We focused our comparison to NeuTra MCMC sampling for a fair comparison, as we only used MADE conditioners in this context, not Jump MCMC. We show the results in Table 6.

The combination of MADE conditioners and NN transformers attains the best \bar{r} across all targets, with C-spline models ranking second. Interestingly, C-spline models rank better than C-NN models, and MADE-NN spline models are better than MADE-spline models. This suggests that autoregressive NF performance in NeuTra MCMC should be assessed by jointly observing the conditioner and transformer, as certain combinations like MADE-NN and C-spline may possess better inductive biases than others.

Combination	Gaussian	Non-Gaussian	Multimodal	Real-world	All
C-Affine	-0.44 ± 0.28	0.88	0.59 ± 0.17	-0.37 ± 0.32	0.46 ± 0.23
C-Spline	-0.59 ± 0.56	-0.59 ± 0.88	-0.44 ± 0.65	-0.15 ± 0.04	-0.49 ± 0.18
C-NN	1.17 ± 0.29	-0.88	0.88 ± 0.41	0.37 ± 0.37	0.29 ± 0.26
MADE-Affine	0.44 ± 0.44	1.46	-0.15 ± 0.05	0.22 ± 0.46	0.52 ± 0.02
MADE-Spline	-0.73 ± 0.37	0.00 ± 0.29	-0.59 ± 0.38	0.15 ± 0.24	-0.23 ± 0.22
MADE-NN	0.15 ± 0.55	-0.88 ± 0.59	-0.29 ± 0.63	-0.22 ± 0.36	-0.55 ± 0.22

Table 6: $\bar{r} \pm \hat{\sigma}$ for all conditioner-transformer combinations in autoregressive NFs, estimated with default hyperparameters for each benchmark. NN denotes neural network transformers, and C denotes coupling conditioners. The top 20% combinations are shown in bold. Ranks are computed separately for each target family.

Nevertheless, MADE models seem to rank somewhat better than models with coupling conditioners, which is consistent with our previous findings in Tables 3 and 5. There are some caveats to this conclusion when observing individual target families:

- On non-Gaussian targets, MADE-NN achieves the best \bar{r} , but has a very high uncertainty. Its performance is matched by C-NN, which always ranks the same on the non-Gaussian target family. The true performance of MADE is thus inconclusive. However, we notice that NN transformers are the best in both cases.
- On multimodal targets, all MADE configurations achieve $\bar{r} < 0$, which indicates good performance. C-spline models could also be promising candidates, however their uncertainty is high.
- On real-world targets, only MADE-NN achieves $\bar{r} < 0$ and is outperformed by C-affine models. We again note the high uncertainty which prevents us from making definitive conclusions.

We further compare the two conditioners by observing the percentage of NeuTra MCMC experiments with identical configurations except for the conditioner. Configurations include the choice of sampler (NeuTra HMC or NeuTra MH), transformer (as defined in Section 3.2), target distribution, and NF hyperparameters. We find that MADE conditioners perform somewhat better, beating coupling conditioners 61% of the time when using affine transformers, 52% with splines, 56% with NN transformers, and 56% of the time across all transformers.

A.3 Experiments with a small time budget

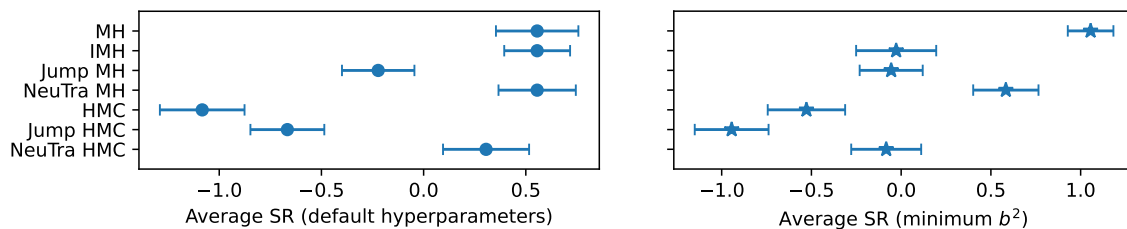
We investigate sampling quality when substantially reducing both the allotted warm-up and sampling time. These experiments are indicative of short-run NFMC performance and can provide useful guidelines when adopting NFMC into mainstream programming packages for sampling, as many of their users typically only deal with quick analyses. We limit warm-up time to 2 minutes and sampling time to 5 minutes.

A.3.1 SAMPLER COMPARISON ON SHORT NFMC RUNS

We present SR values for different samplers in Figures 7a and 7b. We observe some differences in comparison to Figures 1a and 1b.

HMC expectedly performs better than Jump HMC when using default NF hyperparameters, compared to matching the performance of Jump HMC performance in runs with longer warm-up and sampling stages. Interestingly, the opposite holds when observing minimum b^2 . This suggests that choosing an appropriate NF architecture for sampling can improve moment estimates even with limited computational time. A major practical consequence is that we may perform several short runs of NFMC to gauge the potential of different hyperparameter configurations. This reduces the number of repeated NFMC runs with poor hyperparameter choices, which is particularly promising for experiments with long chains or computationally expensive target density evaluations. An extensive hyperparameter search may not be a priority for all analyses. Our results encourage the development of hyperparameter tuning methods for such cases.

When using default NF hyperparameters, IMH and NeuTra MH are comparable to MH, while Jump MH remains the best of the investigated gradient-free samplers. These results suggest that gradient-free sampling can greatly benefit from independent NF jumps even without hyperparameter tuning, which is especially useful for quick tests. IMH and Jump MH are comparable when considering minimum b^2 . As long as the NF architecture and hyperparameters are chosen well, this suggests that independent NF jumps can be more effective than local MH exploration with minimal hyperparameter tuning effort.



(a) $\bar{r} \pm \hat{\sigma}$ across all targets and NFs for each sampler, using b^2 limited to experiments with default NF hyperparameters. Each experiment consisted of two minutes of warm-up and five minutes of sampling.

(b) $\bar{r} \pm \hat{\sigma}$ across all targets and NFs for each sampler, values estimated with minimum b^2 across all NF hyperparameter sets. Each experiment consisted of two minutes of warm-up and five minutes of sampling.

We further investigate sampler performance for different target families in Table 7. Jump HMC is again the decisive winner, just as in longer NFMC runs (see Table 1). Jump MH narrowly remains the best gradient-free sampler overall, only beaten by IMH on real-world targets. The main difference compared to longer NFMC runs is that MH and HMC rank noticeably better on short runs. This is reasonable, as longer runs allow better NF fits. Moreover, there is greater uncertainty in SR for non-Gaussian targets. Jump MH also achieves a worse rank on non-Gaussian targets compared to longer runs. The takeaway is that short-run NFMC is not necessarily suitable for challenging non-Gaussian targets, especially if selecting a suitable NF is very time-consuming.

A.3.2 NF COMPARISON ON SHORT NFMC RUNS

We compare different NF architectures on short Jump MCMC runs in Table 8. We find $\text{CNF}_{\text{RK}(\text{R})}$ to be in the top 20% for all target families, including Gaussian and real-world

Sampler	Gaussian	Non-Gaussian	Multimodal	Real-world	All
MH	1.00 ± 0.20	0.75 ± 0.75	0.75 ± 0.32	1.31 ± 0.13	1.06 ± 0.13
IMH	0.62 ± 0.52	0.5 ± 1.0	0.12 ± 0.24	-0.56 ± 0.29	-0.03 ± 0.22
Jump MH	-0.25 ± 0.32	-0.50 ± 0.50	-0.38 ± 0.12	0.31 ± 0.31	-0.06 ± 0.18
NeuTra MH	0.88 ± 0.31	1.0	0.75 ± 0.60	0.25 ± 0.23	0.58 ± 0.18
HMC	-1.12 ± 0.12	0.00 ± 0.50	-0.38 ± 0.62	-0.44 ± 0.35	-0.53 ± 0.22
Jump HMC	-1.25 ± 0.25	-1.5	-0.88 ± 0.62	-0.69 ± 0.33	-0.94 ± 0.21
NeuTra HMC	0.12 ± 0.24	-0.25 ± 0.75	0.00 ± 0.54	-0.19 ± 0.33	-0.08 ± 0.19

Table 7: $\bar{r} \pm \hat{\sigma}$ for all samplers and target families given 2 minutes of warm-up time and 5 minutes of sampling time. Samplers with the best \bar{r} are shown in bold for each target family. We estimate $\bar{r} \pm \hat{\sigma}$ with the minimum b^2 across all NFs for each target within a family. Entries without $\hat{\sigma}$ always attain the same \bar{r} . Ranks are computed separately for each target family.

targets, where it performed worse during long runs. $\text{CNF}_{\text{Euler}}$ and CNF_{RK} NFs attain $\bar{r} > 0$ on Gaussians, which is similar to the long run results in Table 2, where we only observed $\bar{r} > 0$ on Gaussians with $\text{CNF}_{\text{Euler}}$ and CNF_{RK} . However, the combined ranks suggest that continuous NF models are consistently among the best choices regardless of the allotted computational time. This implies that continuous NF models are among the quickest to efficiently train with few training samples from NFMC.

The main difference regarding autoregressive NFs is the good performance of C-LR-NSF, which ranks second best among all NFs. LRS transformers have more parameters than affine maps in NICE and Real NVP, yet fewer than RQS and NAF transformers. This suggests that the LRS capacity is most beneficial for short runs of Jump MCMC. We also find residual NFs to perform worse on short runs, suggesting that their applicability is somewhat limited.

We compare NFs for short NeuTra MCMC runs in Table 9. The radial flow shows the most striking change in performance. Whereas it decisively ranked best on long NFMC runs (c.f. Table 3), it is among the worst here and clearly the worst choice for Gaussian and synthetic non-Gaussian targets. When considering the entire benchmark, all coupling NFs rank better than in long runs. Their relative ranks remain similar on Gaussian and synthetic non-Gaussian targets but mostly change on multimodal and real-world targets. It is difficult to draw conclusions for the latter two families due to the high uncertainty. We find that C-NAF_{dense} and C-NAF_{both} attain $\bar{r} < 0$ on all families, which contributes to them ranking well on the entire benchmark. The overall ranks of IA methods are largely the same as in long runs, except for worse rankings attained by IA-NAF_{dense} and IA-NAF_{both}. Both residual architectures rank worse than in long runs.

A.3.3 SHORT SUMMARY OF FINDINGS

One of our key findings is that NFMC can still perform well even without long warm-up and tuning stages. For gradient-free sampling, we found Jump MH to perform better than all other gradient-free samplers just by using default NF hyperparameters. This makes it a good primary choice of sampler for short sampling runs. For gradient-based sampling, we found HMC to perform best compared to NFMC with default hyperparameters. If we

NF	Gaussian	Non-Gaussian	Multimodal	Real-world	All
NICE	-0.87 ± 0.34	0.14 ± 0.87	-0.22 ± 0.45	0.29 ± 0.35	-0.10 ± 0.23
Real NVP	-0.22 ± 0.14	-0.29 ± 0.72	-0.22 ± 0.38	-0.33 ± 0.37	-0.27 ± 0.19
C-LR-NSF	-0.58 ± 0.28	0.00 ± 0.14	-0.58 ± 0.60	-0.58 ± 0.20	-0.51 ± 0.16
C-RQ-NSF	-1.16 ± 0.34	1.30 ± 0.29	-0.29 ± 0.34	0.36 ± 0.42	-0.02 ± 0.27
C-NAF _{deep}	0.29 ± 0.34	0.0 ± 1.3	-0.07 ± 0.62	0.80 ± 0.26	0.40 ± 0.23
C-NAF _{dense}	1.3	0.72 ± 0.58	0.87 ± 0.43	0.87 ± 0.20	0.95 ± 0.14
C-NAF _{both}	1.59	0.4 ± 1.2	1.59	0.80 ± 0.36	1.11 ± 0.21
i-ResNet	-0.43 ± 0.20	0.00 ± 0.43	0.07 ± 0.36	-0.47 ± 0.27	-0.29 ± 0.16
ResFlow	0.29 ± 0.36	0.29 ± 0.43	0.14 ± 0.35	-0.58 ± 0.23	-0.13 ± 0.17
CNF _{Euler}	0.80 ± 0.14	-1.45 ± 0.14	-0.51 ± 0.49	-0.47 ± 0.32	-0.31 ± 0.23
CNF _{RK}	0.07 ± 0.46	-0.4 ± 1.2	0.00 ± 0.51	0.04 ± 0.37	-0.02 ± 0.23
CNF _{RK(R)}	-1.09 ± 0.42	-0.72 ± 0.29	-0.80 ± 0.52	-0.72 ± 0.28	-0.82 ± 0.18

Table 8: $\bar{r} \pm \hat{\sigma}$ for all NFs and target families in IMH, Jump MH, and Jump HMC given 2 minutes of warm-up time and 5 minutes of sampling time. NFs in the top 20th percentile are shown in bold for each target family. We estimate $\bar{r} \pm \hat{\sigma}$ with b^2 from runs with default hyperparameters. Entries without $\hat{\sigma}$ always attain the same \bar{r} . Ranks are computed separately for each target family.

choose good hyperparameters, Jump HMC will rank best among gradient-based samplers. The best architectures for it are CNF_{RK(R)}, C-LR-NSF, and CNF_{Euler}. In many cases, we can afford some NF hyperparameter tuning time, which makes Jump HMC a suitable choice for gradient-based sampling.

Appendix B. Experiment details

We provide experiment details, including used hardware, sampler warm-up procedures, NF training details, and NF hyperparameter choices.

B.1 Hardware configuration

Unless otherwise noted, we ran all experiments with the AMD EPYC 7702P CPU. To estimate ground truth moments, we ran standard HMC (without NF extensions) with 100 parallel chains for 20 hours. For each experiment, we ran warm-up for 3 hours and sampling for 7 hours, using 8 GB of memory. The total sequential computation time for the experiments in this paper was roughly 5 to 6 years (not accounting for repeated runs).

B.2 MCMC and NFMC warm-up

We warmed up MH and HMC by sampling while adapting their parameters. We adapted HMC step size with dual averaging, mass matrices in each sampler by $M_{t+1}^{-1} = M_t^{-1} + \sqrt{\text{Cov}[x_t]} \cdot 0.999^t$, where x_t are the current chain states. NeuTra MCMC first performs stochastic variational inference for as long as possible (at most 3 hours), then we warm up the inner MCMC sampler on the adjusted log density and obtain MCMC samples. Jump MCMC has the same warm-up procedure as NeuTra MCMC, except that we also fit the NF again to samples from the MCMC fit.

NF	Gaussian	Non-Gaussian	Multimodal	Real-world	All
NICE	-0.70 ± 0.41	0.74 ± 0.08	-0.58 ± 0.46	-0.23 ± 0.31	-0.30 ± 0.21
Real NVP	-0.50 ± 0.40	0.74 ± 0.41	0.41 ± 0.27	-0.15 ± 0.33	0.00 ± 0.20
C-LR-NSF	-1.03 ± 0.24	0.50 ± 0.17	-0.08 ± 0.47	-0.20 ± 0.38	-0.28 ± 0.22
C-RQ-NSF	-0.58 ± 0.27	-0.91 ± 0.74	-0.54 ± 0.53	0.36 ± 0.31	-0.22 ± 0.22
C-NAF _{deep}	0.58 ± 0.26	0.00 ± 0.17	0.74 ± 0.46	0.51 ± 0.32	0.52 ± 0.18
C-NAF _{dense}	-0.37 ± 0.61	-1.32 ± 0.17	-0.08 ± 0.60	-0.56 ± 0.36	-0.50 ± 0.24
C-NAF _{both}	-0.41 ± 0.64	-1.32 ± 0.17	-0.45 ± 0.57	-0.28 ± 0.38	-0.47 ± 0.25
IAF	-0.50 ± 0.36	1.16 ± 0.17	-0.29 ± 0.37	0.51 ± 0.32	0.18 ± 0.22
IA-LR-NSF	-0.50 ± 0.39	0.25 ± 0.25	-0.12 ± 0.37	-0.19 ± 0.21	-0.19 ± 0.15
IA-RQ-NSF	-0.83 ± 0.26	-0.08 ± 0.25	-0.21 ± 0.54	-0.44 ± 0.28	-0.43 ± 0.18
IA-NAF _{deep}	-0.41 ± 0.49	-0.5	-0.41 ± 0.14	-0.59 ± 0.35	-0.50 ± 0.18
IA-NAF _{dense}	0.12 ± 0.55	0.00 ± 0.99	0.74 ± 0.43	0.75 ± 0.22	0.53 ± 0.20
IA-NAF _{both}	1.16 ± 0.07	-0.17 ± 0.66	1.45 ± 0.04	0.74 ± 0.37	0.90 ± 0.20
i-ResNet	-0.12 ± 0.30	-0.50 ± 0.17	-0.12 ± 0.54	-0.52 ± 0.29	-0.34 ± 0.18
ResFlow	-0.50 ± 0.43	-0.74 ± 0.08	0.08 ± 0.37	-0.39 ± 0.34	-0.35 ± 0.19
Planar	0.04 ± 0.26	0.41 ± 0.41	0.12 ± 0.35	-0.54 ± 0.28	-0.16 ± 0.17
Radial	1.65	1.65	0.83 ± 0.83	-0.03 ± 0.46	0.72 ± 0.31
Sylvester	-0.41 ± 0.21	0.1 ± 1.4	-0.58 ± 0.14	-0.22 ± 0.22	-0.34 ± 0.19
CNF _{Euler}	1.49	0.3 ± 1.2	-0.62 ± 0.71	0.90 ± 0.35	0.62 ± 0.29
CNF _{RK}	1.28 ± 0.04	0.0 ± 1.3	-0.45 ± 0.66	0.60 ± 0.43	0.45 ± 0.29
CNF _{RK(R)}	0.54 ± 0.41	-0.3 ± 1.4	0.17 ± 0.54	-0.08 ± 0.36	0.09 ± 0.24

Table 9: $\bar{r} \pm \hat{\sigma}$ for all NFs and target families in NeuTra MH and NeuTra HMC given 2 minutes of warm-up time and 5 minutes of sampling time. NFs in the top 20th percentile are shown in bold for each target family. We estimate $\bar{r} \pm \hat{\sigma}$ with b^2 from runs with default hyperparameters. Entries without $\hat{\sigma}$ always attain the same \bar{r} . Ranks are computed separately for each target family.

B.3 NF training details

In maximum likelihood fitting (i.e., given training samples), we trained all NFs with the Adam optimizer, step size 0.05 and batch size 1024. When given a validation set (in maximum likelihood fitting), we stopped training after no validation loss improvement in 5000 consecutive steps. In SVI, we stopped training after 5000 steps of no training loss improvement. We kept the best weights according to validation loss in both cases. We used a single sample in SVI.

At the time of writing, Agrawal and Domke (2024) performed a study of SVI for the Real NVP architecture. They observe that large batch sizes reduce gradient variance and thus improve fit quality. They observe a similar effect when using a reduced variance gradient estimator, however they state that it is impractical for NFs with expensive bijection inversion costs. Our preliminary tests showed that large batch sizes and the reduced variance estimator take up a large chunk of the computational budget for certain NFs due to very slow autodifferentiation, thus negatively impacting their performance. Applying large batch sizes and the estimator to only select NFs would prevent a fair comparison and potentially add excessive variation to our results. We thus avoid these two approaches in SVI fits. Our choice promotes a fair comparison because the fitting routines are identical for all NFs.

B.4 NF hyperparameter choices

We set NF hyperparameters such that all NFs successfully passed a series of automated tests, which ensured numerical stability in the following aspects:

- We reconstruct an input by first passing it to the forward bijection method, then the inverse bijection method. The reconstruction error must not be too great.
- No trainable parameter or the loss may take on a NaN value during forward passes, inverse passes, and loss gradient computation.

For autoregressive NFs, we use the following hyperparameter combinations:

- We used 2, 5, or 10 bijective layers in the composition.
- We used either conditioner hidden size 10 and two conditioner layers or conditioner hidden size 100 and five conditioner layers.

We split input tensors in half across the first dimension for coupling NFs. We used the Tanh activation in all conditioners, as it ensured controllable magnitudes of outputs. We noticed that the ReLU activation can result in predicting parameters in large magnitudes, which causes divergences in NFMC. We used 8 splines in all LRS and RQS transformers. For NAF, we used one dense layer with 8 neurons for NN_{dense} , two hidden layers with hidden size $\max(5\lceil\log_{10} d\rceil, 4)$ in NN_{deep} , and two layers with 8 neurons in NN_{both} . For Sylvester flows, we used $m = \frac{d}{2}$ columns in Q for the QR decomposition. We used 2, 5, and 10 layers in matrix determinant residual NFs. For contractive residual NFs, we used a spectrally normalized neural network with 1 hidden layer, $3\max(\lceil\log_{10} d\rceil, 4)$ hidden neurons, and TanH activations. We used $p = 0.5$ for the Roulette estimator in ResFlow. To parameterize g_ϕ in continuous NFs, we used 1, 5, or 10 hidden layers with 10 or 100 hidden neurons. We implement time-dependence in g_ϕ for $\text{CNF}_{\text{RK(R)}}$ and CNF_{RK} by concatenating the time variable to the remainder of the input. Any other hyperparameter choices can be found in the linked repositories.

Appendix C. Sampler definitions

In this section, we define each investigated MCMC sampler.

C.1 Metropolis-Hastings

The Metropolis-Hastings sampler defines its proposal and log acceptance ratio as follows:

$$\begin{aligned} x'_{t+1} &= x_t + M^{-1}u_t, \quad u_t \sim N(0, I), \\ \log \alpha_t &= \log p(x'_t) - \log p(x_t). \end{aligned}$$

Here, x_t is the current state, x'_{t+1} is the proposed next state, M^{-1} is the inverse of the diagonal mass matrix. We set $x_{t+1} = x'_{t+1}$ if $\log \alpha_t > \log w_t, w_t \sim U(0, 1)$, otherwise we set $x_{t+1} = x_t$.

C.2 Hamiltonian Monte Carlo

Hamiltonian Monte Carlo (with the leapfrog integrator) defines each trajectory step as:

$$\begin{aligned} r^{(k+1/2)} &= r^{(k)} + h/2\nabla \log p(x^{(k)}), \\ x^{(k+1)} &= x^{(k)} + hM^{-1}r^{(k+1/2)}, \\ r^{(k+1)} &= r^{(k+1/2)} + h/2\nabla \log p(x^{(k+1)}). \end{aligned}$$

Here, $x^{(k)}, r^{(k)}$ are the current trajectory state and momentum, $x^{(k+1)}, r^{(k+1)}$ are the next trajectory state and momentum, $r^{(k+1/2)}$ is the intermediate momentum, M^{-1} is the inverse of the diagonal mass matrix. The trajectory has $L > 0$ steps with $r^{(1)} = M^{-1}u, u \sim N(0, I)$. The proposed next state and log acceptance ratio are defined as:

$$\begin{aligned} x'_{t+1} &= x_t^{(L)}, \\ \log \alpha_t &= \log p(x'_{t+1}) - \log p(x_t) - 0.5 \left(r_t^{(L)\top} M^{-1} r_t^{(L)} - r_t^{(1)\top} M^{-1} r_t^{(1)} \right). \end{aligned}$$

The momentum $r^{(1)}$ is refreshed at the beginning of each trajectory by newly sampling $u \sim N(0, I)$. We set the new state as in subsection C.1.

C.3 NeuTra MCMC

NeuTra MCMC uses an NF $q(x)$ with the bijection f that maps a data space point x to a latent space point $z = f(x)$. Given a target distribution p , it runs an MCMC sampler with the transformed target log density:

$$\log \tilde{p}(x) = \log p(f(x)) + \log \left| \det \left(\frac{\partial f(x)}{\partial x} \right) \right|.$$

We set the new state as in subsection C.1.

C.4 Jump MCMC and IMH

Every K -th step of Jump MCMC with an NF $q(x)$ proposes a new state as in Equation 2 and computes the log acceptance ratio as in Equation 3. We set the new state as in subsection C.1. Other steps are performed with an MCMC sampler. When $K = 1$, Jump MCMC reduces to IMH.

Appendix D. Benchmark distribution details

In this section, we give precise definitions for all target distributions in our benchmark. We parameterize univariate Gaussian and half-Cauchy distributions with the standard deviation (not the variance).

D.1 Synthetic Gaussian target distributions

We use the following Gaussian distributions in our benchmark:

- Standard Gaussian in 100 dimensions.

- Diagonal Gaussian in 100 dimensions with zero mean and standard deviation linearly spaced between 1 and 10.
- Full-rank Gaussian in 100 dimensions with zero mean and eigenvalues $\lambda_1, \dots, \lambda_{100}$ linearly spaced between 1 and 10, giving rise to covariance $\Sigma = Q\Lambda Q^\top$ with $\Lambda = \text{diag}(\lambda_1, \dots, \lambda_{100})$ and Q orthonormal.
- Ill-conditioned full-rank Gaussian in 100 dimensions with zero mean and eigenvalue reciprocals $\lambda_i^{-1} \sim \text{Gamma}(0.5, 1)$, giving rise to covariance $\Sigma = Q\Lambda Q^\top$ with $\Lambda = \text{diag}(\lambda_1, \dots, \lambda_{100})$ and Q orthonormal.

The orthonormal rotation matrix Q is generated by decomposing a 100×100 standard normal matrix A into $Q_0 R = A$ where Q_0 is orthonormal and R is upper triangular. We then proceed with $Q = Q_0 \text{diag}(\text{sign}(\text{diag}(R)))$, which multiplies the diagonal of Q_0 with the sign of the diagonal of R to give Q a determinant of 1, while keeping all off-diagonal elements of Q the same as Q_0 .

D.2 Synthetic non-Gaussian unimodal target distributions

We use the following synthetic non-Gaussian unimodal distributions in our benchmark:

- Funnel distribution in 100 dimensions. The first dimension is given by $N(0, 3)$, all remaining dimensions are given by $x_i | x_1 \sim N(0, \exp(x_1/2))$.
- Rosenbrock banana distribution in 100 dimensions with scale 10.

The un-normalized Rosebrock banana log density for an input $x \in \mathbb{R}^D$ (with D even and scale s) is defined as:

$$\log \tilde{p}(x) = - \sum_{d=1}^{D/2} s(x_{2d-1}^2 - x_{2d})^2 + (x_{2d-1} - 1)^2.$$

D.3 Synthetic multimodal target distributions

We use the following multimodal distributions in our benchmark:

- A mixture with three diagonal Gaussian components in 100 dimensions. Component means are $-5, 0,$ and 5 , respectively, in all dimensions. Component standard deviations are 0.7 in all dimensions. Component weights are $1/3$ for all three components.
- A mixture with twenty diagonal Gaussian components in 100 dimensions. Component means are randomly sampled from $N(0, 10)$ in all dimensions. Component standard deviations are 1 in all dimensions. Component weights given by $\text{softmax}(x_1, \dots, x_{20})$ where $x_i \sim N(0, 1)$.
- A double well distribution in 10 dimensions (containing 2^{10} modes).
- A double well distribution in 100 dimensions (containing 2^{100} modes).

The un-normalized double well log density for an input $x \in \mathbb{R}^D$ is defined as

$$\log \tilde{p}(x) = - \sum_{d=1}^D (x^2 - 4)^2.$$

D.4 Real-world target distributions

We define the real-world target distributions included in our benchmark. We acquire data for likelihood functions from the repository by Magnusson et al. (2024).

D.4.1 EIGHT SCHOOLS

Given a parameter vector $(\mu, \tilde{\tau}, \theta')$ with $\mu \in \mathbb{R}$, $\tilde{\tau} \in \mathbb{R}$, $\theta' \in \mathbb{R}^8$ and measurements $y_i \in \mathbb{R}$, $\sigma_i > 0, i = 1, \dots, 8$, the 10D eight schools model defined as:

$$\begin{aligned} \tau &= \log(1 + \exp(\tilde{\tau})), \quad \theta = \mu + \tau\theta', \\ \mu &\sim N(0, 10), \quad \tau \sim \text{LogNormal}(5, 1), \quad \theta'_i \sim_{iid} N(0, 1), \\ y_i &\sim N(\theta_i, \sigma_i). \end{aligned}$$

D.4.2 GERMAN CREDIT

Given a parameter vector $(\tilde{\tau}, \beta)$ with $\tilde{\tau} \in \mathbb{R}$, $\beta \in \mathbb{R}^{25}$ and measurements (x_j, y_j) with $x_j \in \mathbb{R}^{25}$, $y_j \in \{0, 1\}$, the 26D German credit model is defined as:

$$\begin{aligned} \tau &= \log(1 + \exp(\tilde{\tau})), \\ \tau &\sim \text{Gamma}(0.5, 0.5), \quad \beta_i \sim_{iid} N(0, 1), \\ y_j &\sim \text{Bernoulli}(\sigma(\tau\beta^\top x_j)). \end{aligned}$$

We use the shape-rate parameterization for the Gamma distribution. Bernoulli parameters are computed with the sigmoid function σ .

D.4.3 SPARSE GERMAN CREDIT

Given a parameter vector $(\tilde{\tau}, \tilde{\lambda}, \beta)$ with $\tilde{\tau} \in \mathbb{R}$, $\tilde{\lambda} \in \mathbb{R}^{25}$, $\beta \in \mathbb{R}^{25}$ and measurements (x_j, y_j) with $x_j \in \mathbb{R}^{25}$, $y_j \in \{0, 1\}$, the 51D sparse German credit model is defined as:

$$\begin{aligned} \tau &= \log(1 + \exp(\tilde{\tau})), \quad \lambda = \log(1 + \exp(\tilde{\lambda})), \\ \tau, \lambda_i &\sim_{iid} \text{Gamma}(0.5, 0.5), \quad \beta_i \sim_{iid} N(0, 1), \\ y_j &\sim \text{Bernoulli}(\sigma(\tau(\beta\lambda)^\top x_j)). \end{aligned}$$

We use the shape-rate parameterization for the Gamma distribution. The product between β and λ is element-wise multiplication. Bernoulli parameters are computed with the sigmoid function σ .

D.4.4 RADON (VARYING INTERCEPTS)

Given a parameter vector $(\mu_b, \tilde{\sigma}_b, \tilde{\sigma}_y, a, b)$ with $\mu_b, \tilde{\sigma}_b, \tilde{\sigma}_y, a \in \mathbb{R}$, $b \in \mathbb{R}^{85}$ and measurements (r_j, f_j) with $r_j \in \mathbb{R}$, $f_j \in \{0, 1\}$, the 89D radon model with varying intercepts is defined as:

$$\begin{aligned} \sigma_b &= \log(1 + \exp(\tilde{\sigma}_b)), \quad \sigma_y = \log(1 + \exp(\tilde{\sigma}_y)) \\ \mu_b, a &\sim N(0, 10^5), \quad \sigma_b, \sigma_y \sim \text{HalfCauchy}(5), \quad b_i \sim_{iid} N(\mu_b, \sigma_b), \\ r_j &\sim N(af_{c(j)} + b_{c(j)}, \sigma_y). \end{aligned}$$

Here, $c(j)$ is the county associated with the data point at index j .

D.4.5 RADON (VARYING SLOPES)

Given a parameter vector $(\mu_a, \tilde{\sigma}_a, \tilde{\sigma}_y, a, b)$ with $\mu_a, \tilde{\sigma}_a, \tilde{\sigma}_y, b \in \mathbb{R}, a \in \mathbb{R}^{85}$ and measurements (r_j, f_j) with $r_j \in \mathbb{R}, f_j \in \{0, 1\}$, the 89D radon model with varying intercepts is defined as:

$$\begin{aligned} \sigma_a &= \log(1 + \exp(\tilde{\sigma}_a)), \quad \sigma_y = \log(1 + \exp(\tilde{\sigma}_y)) \\ \mu_a, b &\sim N(0, 10^5), \quad \sigma_a, \sigma_y \sim \text{HalfCauchy}(5), \quad a_i \sim_{iid} N(\mu_a, \sigma_a), \\ r_j &\sim N(a_{c(j)}f_{c(j)} + b, \sigma_y). \end{aligned}$$

Here, $c(j)$ is the county associated with the data point at index j .

D.4.6 RADON (VARYING INTERCEPTS AND SLOPES)

Given a parameter vector $(\mu_a, \tilde{\sigma}_a, \tilde{\sigma}_y, a, b)$ with $\mu_a, \tilde{\sigma}_a, \tilde{\sigma}_y, a, b \in \mathbb{R}^{85}$ and measurements (r_j, f_j) with $r_j \in \mathbb{R}, f_j \in \{0, 1\}$, the 175D radon model with varying intercepts and slopes is defined as:

$$\begin{aligned} \sigma_a &= \log(1 + \exp(\tilde{\sigma}_a)), \quad \sigma_b = \log(1 + \exp(\tilde{\sigma}_b)), \quad \sigma_y = \log(1 + \exp(\tilde{\sigma}_y)) \\ \mu_a, \mu_b &\sim N(0, 10^5), \quad \sigma_a, \sigma_b, \sigma_y \sim \text{HalfCauchy}(5), \quad a_i \sim_{iid} N(\mu_a, \sigma_a), \quad b_i \sim_{iid} N(\mu_b, \sigma_b), \\ r_j &\sim N(a_{c(j)}f_{c(j)} + b_{c(j)}, \sigma_y). \end{aligned}$$

Here, $c(j)$ is the county associated with the data point at index j .

D.4.7 SYNTHETIC ITEM RESPONSE THEORY

Given a parameter vector (α, β, δ) with $\alpha \in \mathbb{R}^{400}, \beta \in \mathbb{R}^{100}, \delta \in \mathbb{R}$ and measurements $y_k \in \{0, 1\}$, the 501D synthetic item response theory model is defined as:

$$\begin{aligned} \delta &\sim N(0.75, 1), \quad \alpha_i, \beta_j \sim_{iid} N(0, 1) \\ y_k &\sim \text{Bernoulli}(\sigma(\alpha_{s(k)} - \beta_{r(k)} + \delta)) \end{aligned}$$

Here, $s(k)$ is the student, and $r(k)$ is the response associated with the data point at index k . Bernoulli parameters are computed with the sigmoid function σ .

D.4.8 STOCHASTIC VOLATILITY

Given a parameter vector $(z, \tilde{\sigma}, \tilde{\mu}, \tilde{\phi}')$ with $z \in \mathbb{R}^{3000}; \tilde{\sigma}, \tilde{\mu}, \tilde{\phi}' \in \mathbb{R}$ and measurements $y_i \in \mathbb{R}$, the 3003D stochastic volatility model is defined as:

$$\begin{aligned} \sigma &= \log(1 + \exp(\tilde{\sigma})), \quad \mu = \log(1 + \exp(\tilde{\mu})), \quad \phi' = 1/(1 + \exp(-\tilde{\phi}')), \quad \phi = 2\phi' - 1, \\ h_1 &= \mu + \sigma z_1 - \sqrt{1 - \phi^2}, \quad h_i = \mu + \sigma z_i + \phi(h_{i-1} - \mu) \text{ for } i > 1, \\ z_i &\sim_{iid} N(0, 1), \quad \sigma \sim \text{HalfCauchy}(2), \quad \mu \sim \text{Exp}(1), \quad \phi' \sim \text{Beta}(20, 1.5), \\ y_i &\sim N(0, \exp(h_i/2)). \end{aligned}$$

Appendix E. Comparison metric definitions

In this section, we define the squared bias of the second moment and the standardized rank.

E.1 Squared bias of the second moment

Let X be the random variable corresponding to a target distribution, and X_d its d -th dimension. Let $\mathbb{E}[X_d^2]$ be the true d -th marginal second moment and $\text{Var}[X_d]$ the true d -th marginal variance of the target distribution. Let $\tilde{\mathbb{E}}[X_d^2]$ be the estimated second moment of X_d , obtained using MCMC samples $x^{(i,j)}$ from n MCMC steps and m independent chains:

$$\tilde{\mathbb{E}}[X_d^2] = \frac{1}{nm} \sum_{i=1}^n \sum_{j=1}^m \left(x_d^{(i,j)}\right)^2.$$

We measure the error in estimating a distribution's moments with the squared bias of the second moment:

$$b^2 = \max_d \frac{\left(\tilde{\mathbb{E}}[X_d^2] - \mathbb{E}[X_d^2]\right)^2}{\text{Var}[X_d]}.$$

The minimum possible value of b^2 is zero when the estimated second moment exactly matches the true second moment. In practice, we observe non-negative values of b^2 . If one sampler attains lower b^2 than another on a target distribution, we deem it better for second moment estimation on that distribution.

E.2 Standardized rank

Suppose we rank sampling methods m_1, \dots, m_K on a single target according to b^2 , obtaining ranks r_1, \dots, r_K . Sampling methods include MCMC samplers, NFs, or both. We obtain standardized ranks by subtracting the empirical mean and dividing by the standard deviation:

$$r_{s,i} = \frac{r_i - \tilde{\mu}}{\tilde{\sigma}}, \text{ where } \tilde{\mu} = \frac{1}{K} \sum_{i=1}^K r_i \text{ and } \tilde{\sigma} = \sqrt{\frac{1}{K-1} \sum_{i=1}^K (r_i - \tilde{\mu})^2}.$$

If we compute $r_{s,i}$ for different targets $j = 1, \dots, B$, we can observe their empirical distribution. We can also estimate the mean and the standard error of the mean:

$$\overline{r_{s,i}} = \frac{1}{B} \sum_{j=1}^B r_{s,i}^{(j)} \text{ and } \hat{\sigma}_{s,i} = \frac{\sigma_{s,i}}{\sqrt{B}}, \text{ where } \sigma_{s,i} = \sqrt{\frac{1}{B-1} \sum_{j=1}^B \left(r_{s,i}^{(j)} - \overline{r_{s,i}}\right)^2}.$$

We construct a confidence interval for $\overline{r_{s,i}}$ as $(\overline{r_{s,i}} - \hat{\sigma}_{s,i}, \overline{r_{s,i}} + \hat{\sigma}_{s,i})$. This interval defines uncertainty in estimating $\overline{r_{s,i}}$. The smaller the interval, the more confident we are in our estimate of $\overline{r_{s,i}}$.

Appendix F. Memory-efficient moment estimation

Estimating moments of high-dimensional targets by averaging all acquired samples is computationally inefficient and causes out-of-memory errors on longer runs. Instead, we implemented a running-average approach for moment estimation. Suppose we are at step m of

an MCMC run. We have already used samples x_1, \dots, x_m to compute the current running average, and we wish to use samples x_{m+1}, \dots, x_n to update the running average. We derive the empirical running average $\mathbb{E}_{1:n}[f(x)]$ of a statistical functional f with transformed data point $f_i = f(x_i)$ as follows:

$$\begin{aligned} \mathbb{E}_{1:n}[f(x)] &= \frac{1}{n} \sum_{i=1}^n f_i = \frac{1}{n} \sum_{i=1}^m f_i + \frac{1}{n} \sum_{i=m+1}^n f_i \\ &= \frac{m}{n} \frac{1}{m} \sum_{i=1}^m f_i + \frac{n-m}{n} \frac{1}{n-m} \sum_{i=m+1}^n f_i \\ &= \frac{m}{n} \mathbb{E}_{1:m}[f(x)] + \frac{n-m}{n} \mathbb{E}_{m+1:n}[f(x)]. \end{aligned}$$

We thus weigh the previous average and the average of the incoming batch of samples. The space complexity of the estimate is bounded by the size of the sample batch, which is usually just one data point of size equal to the target dimensionality for each chain. We estimate the first moment with $f(x) = x$ and the second moment with $f(x) = x^2$.

F.1 Efficient NeuTra moments

In its original formulation, NeuTra MCMC samples all points in the latent space and then transforms them back to the original space once sampling has finished. To avoid excessive memory usage, we instead reuse the described running moment estimation approach and transform data points with the inverse NF transformation. The functionals thus become $f(x) = \text{inverse}(x)$ for the first moment and $f(x) = \text{inverse}(x)^2$ for the second moment. Note that the inverse only has to be called once. This approach applies the same number of inverse calls as classic NeuTra MCMC but requires constant memory, whereas space requirements otherwise grow with the number of MCMC steps.